Structural, Morphological, Optical and Electro-chemical Study of Er-Intercalated V_2CT_x and $Ti_3C_2T_x$ MXenes for Energy Conversion Applications

Shamaila Fatima

Fall-2020-MS Physics

Reg No: 00000330939

The following thesis is submitted to fulfil the requirement of the degree of **Master of Sciences**

In

Physics

Supervised by

Prof. Dr. Syed Rizwan Hussain

Department of Physics

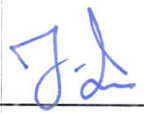School of Natural Sciences (SNS)

National University of Sciences and Technology (NUST)

H-12, Islamabad, Pakistan

Year 2023

National University of Sciences & Technology

MS THESIS WORK

We hereby recommend that the dissertation prepared under our supervision by: **Shamaila Fatima**, Regn No. **00000330939** Titled: **"Structural, Morphological, Optical and Electro-Chemical Study of Er-Intercalated V2CTx and Ti$_3$C$_2$T$_x$ MXenes for Energy Conversion Applications"** accepted in partial fulfillment of the requirements for the award of **MS** degree.

Examination Committee Members

1. Name: DR. FAHEEM AMIN   Signature:

2. Name: DR. ZEESHAN ALI   Signature:

Supervisor's Name: PROF. SYED RIZWAN HUSSAIN   Signature:

_____   23-06-2023
Head of Department   Date

COUNTERSINGED

Date: 23/6/2023   _____
                                    Dean/Principal

DEDICATION

to

Maa & Baba

Acknowledgement

I am profoundly grateful to Allah Almighty for His countless blessings throughout the journey of completing this thesis. His divine support has been the cornerstone of my perseverance and success. I acknowledge that all achievements and accomplishments are ultimately by ALLAH almighty grace.

I would like to express my deepest appreciation to my supervisor, **Prof. Syed Rizwan Hussain**, for their exceptional guidance, unwavering support, and invaluable mentorship. Their expertise, constructive feedback, and dedication to academic excellence have played a pivotal role in shaping the direction and quality of this research. I am sincerely grateful for their patience, wisdom, and encouragement, which have been instrumental in my growth as a researcher.

I would like to express my heartfelt gratitude to the members of the Graduate Examination Committee (GEC), **Dr. Faheem Amin (SNS)** and **Dr. Zeehan Ali (SCME)** NUST, for generously offering their time and invaluable guidance. Their expertise and support have played a significant role in shaping the direction and quality of my research. Additionally, I am grateful to Dr. Rashid Farooq, the principal of the School of Natural Sciences (SNS), Prof. Syed Rizwan Hussain, the Head of the Department of Physics (SNS) for providing a healthy and productive research environment.

I am also indebted to my Adv. 2D Material Devices lab colleagues **Sabeen Fatima, Afsheen Zahra, Rabia Tahir, Waqas Hakim, Zulqurnain Haider, Usmaan Naseem, Ebrima Cessey** and all the other members whose companionship, intellectual discussions, and unwavering support have made this research voyage memorable and enjoyable. The development and refinement of this thesis have been substantially aided by their motivation and willingness to provide feedback.

In addition, I am profoundly appreciative of my family's unconditional affection, constant encouragement, and unwavering support. Their confidence in my skills, insight, and sacrifices has continually motivated and inspired me. I am extremely grateful for their presence in my life and their contribution to my academic success.

Abstract

Two-dimensional (2D) MXenes, also referred to as transition metal carbides/nitrides, exhibit electrocatalytic water-splitting applications due to their unique characteristics. These include a layered structure, high density, metallic-like conductivity, and functional surface groups that help to achieve efficient water splitting for the generation of clean and sustainable hydrogen energy.

This study presents a comprehensive experimental investigation focusing on two different MXenes namely, V_2CT_x and $Ti_3C_2T_x$, and their corresponding nanocomposites, $Er@V_2CT_x$ and $Er@Ti_3C_2T_x$, for their suitability for water-splitting applications. The electrochemical behaviour of the $Er@V_2CT_x$ and $Er@Ti_3C_2T_x$ nanocomposites, with varying percentages of Er incorporated into vanadium carbide and titanium carbide MXene matrices, is extensively studied and discussed. Electrochemical testing was conducted in an alkaline medium (1M KOH) to evaluate hydrogen evolution reaction (HER) and oxygen evolution reaction (OER) potential.

The $Er@V_2CT_x$ nanocomposite exhibited a redox potential of 174 mV at a current density of 10 mA/cm^2, with a Tafel slope of 107 mV/dec for HER. Similarly, the $Er@Ti_3C_2T_x$ nanocomposite demonstrated an overpotential of 256 mV at 10 mA/cm^2 current density, with a Tafel slope of 102 mV/dec for HER. For the OER, the $Er@V_2CT_x$ nanocomposite exhibited an overpotential of 370 mV at 10 mA/cm^2 current density, with a Tafel slope of 131 mV/dec, while the $Er@Ti_3C_2T_x$ nanocomposite showed an overpotential of 381 mV at 10 mA/cm^2 current density, with a Tafel slope of 157 mV/dec. The structure and morphology of the compounds were examined using techniques such as X-ray diffraction (XRD), scanning electron microscopy (SEM), energy dispersion spectroscopy (EDS), Fourier-transform infrared spectroscopy (FTIR), and Raman spectroscopy, confirming the successful formation of the nanocomposites while retaining the desirable two-dimensional (2D) structure of MXene.

Keywords: 2D MXene, Electrocatalysis, overpotential, water splitting, Hydrogen Evolution Reaction, Oxygen Evolution Reaction.

Table of Contents

List of Figures

List of Table

List of Abbreviations

STM   Scanning Tunneling Microscopy

AFM   Atomic Force Microscope

TMDs   Transition metal dichalogenides

GO   Graphene Oxide

rGO   Reduced graphene oxide

XRD   X-ray Diffraction

SEM   Scanning Electron Microscopy

EDX   Energy-Dispersive X-ray

FTIR   Fourier Transform Infrared Spectroscopy

LSV   Linear sweep voltammetry

EIS   Electrochemical Impedance Spectroscopy

HER   Hydrogen Evolution Reaction

OER   Oxygen Evolution Reaction

HF   Hydrofluoric Acid

Chapter 01: Introduction

1.1. Nanoscience and nanotechnology

Nanoscience[1] is the study of the characteristics and behavior of materials between 1 and 100 nanometers in size. This area arose as a result of technological breakthroughs that enabled scientists to alter and examine materials on such a minute scale. The unique features of nanoscale materials[2] have created several new opportunities in industries like medical, electronics, and energy, among others. For instance, nanoparticles can be created to specifically target and eliminate cancer cells without harming healthy cells. Additionally, nanoscale materials can be employed to make more effective solar cells and batteries. In addition, nanoscience research has improved our understanding of the underlying principles that govern the behavior of matter at all sizes. This has enabled scientists to build novel materials with specific qualities and purposes, such as superconductors[3], which have zero electrical resistance[4] and are now being developed for use in sophisticated computer and transportation systems. As nanoscience continues to evolve, it is expected to have an intense influence on our lives by numerous aspects including healthcare and electronics to environmental protection and sustainability. There are additional concerns about the possible risks of using nanomaterials, which need to be carefully studied and dealt with to make sure they are used safely and responsibly.
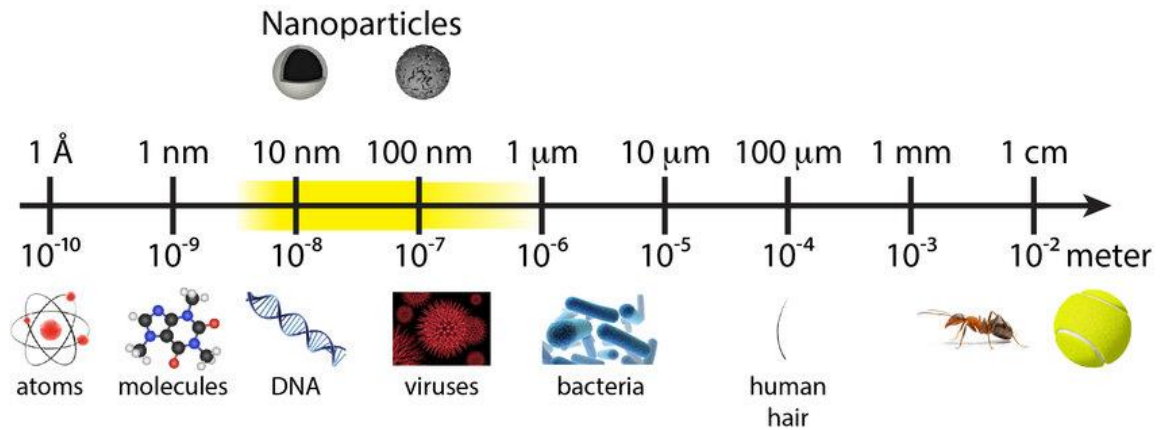
Figure 1.1: Representation of typical sizes of objects and organisms[5].

1.2. History of nanoscience and nanotechnology

Nanotechnology is the science of controlling matter at the atomic and molecular levels. It has roots in physics, chemistry, and biology, among other fields. Richard Feynman first presented the concept of influencing individual atoms and molecules in a 1959 lecture titled:

"There's Plenty of Room at the Bottom."[6]

However, nanotechnology did not really take off until the development and understanding of scanning tunneling microscope (STM) in 1981. Scientists examined and manipulated the atoms and molecules for the first time using STM. The Nobel Prize in Physics had been given to Gerd Binnig and Heinrich Rohrer for the invention of the STM in 1986.

The revelation led to the rapid growth of nanotechnology and K. Eric Drexler coined the phrase in his 1986 book **"Engines of Creation"**. Drexler proposed the concept of constructing tiny devices, which he termed "nanomachines." These machines, he suggested, might have significant uses in industries.[7]

In the 1990s, scientists began to investigate the possible applications of nanotechnology in a variety of industries. In 1986, the atomic force microscope (AFM) was developed[8,9], which was one of the most significant advances. The AFM enabled scientists to manipulate individual atoms and molecules in a controlled manner, opening up new nanotechnology possibilities.

Since then, nanotechnology has expanded and been utilized in numerous fields. Nanotechnology has been contributed in the advancement of more powerful computer chips as well as in smaller size and revolutionize in the domain of electronics industry[10]. In the field of medicine, nanotechnology has been utilized to produce targeted drug delivery systems that can deliver medications directly to cancer cells without harming healthy cells. In the energy field, nanotechnology has led to better solar cells and devices that store energy[11].

Thus, a substantial amount of research and development began with the creation of various promising materials, such as graphene[12] (a carbon-based compound) and MXene[13,14] (2D transition metal carbide), and their vast applicability in a variety of industries.

1.1. How to Approach Nanoscale?

When it comes to approaching nano-sized items, there are two distinct approaches that might be taken. One of them is a **top-down approach**[15] of miniaturizing existing technologies, while the other is a **bottom-up approach**[16] of constructing complicated molecular electronics atom by atom. The top-down approach involves making existing technologies smaller.

According to Britannica Encyclopedia Inc., top-down techniques have been developed for constructing micrometer-scale (μm) structures. On the nanometer (nm) scale, bottom-up strategies for constructing clusters of atoms or molecules have also been created (nm)[17]. The next step is to integrate these strategies to build larger nanoscale structures.

In the assembly of nanoscale devices and structures, the **top-down strategy** is frequently employed. It is the process of creating patterns and structures on a substrate utilizing techniques such as lithography and etching. Typically, the substrate is a bigger material that has been nanoscale-scale patterned. In the semiconductor industry, this method is extensively employed to produce integrated circuits and other electronic devices.

The **bottom-up strategy**, on the other hand, emphasizes the assembling of atoms and molecules into larger structures. Using techniques such as chemical vapor deposition, self-assembly, and colloidal synthesis, atoms or molecules are formed into clusters of nanoparticles. Bottom-up techniques offer the benefit of manufacturing very homogeneous and well-defined nanostructures, but it can be more difficult to scale them up to industrial production levels.
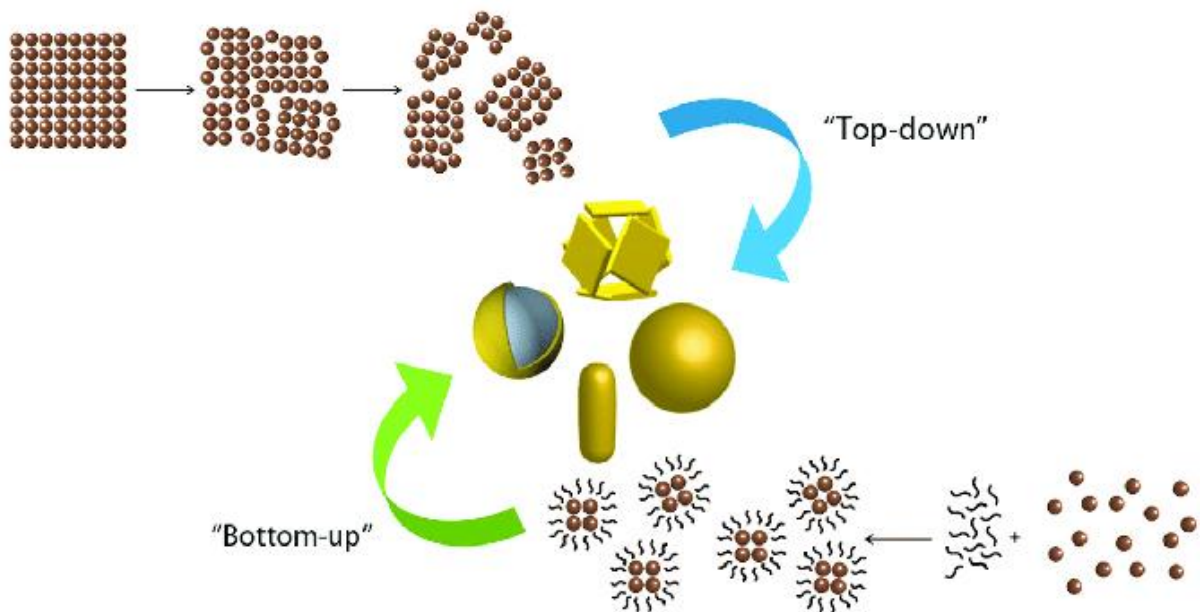
Figure 1.2: Representation for preparation of nanomaterials by following top-down and bottom-up approaches[18].

In recent years, the development of nano-hybrid materials has become interesting for researchers that combines the best parts of both top-down and bottom-up approaches[19]. For example, researchers have come up with ways to use top-down fabrication strategies to

make templates for bottom-up assembly. This makes it possible to make very precise nanostructures with sizes and shapes that can be controlled.

1.2. Nanomaterials

Nanomaterials are substances whose dimensions fall inside the nanoscale range. They may be composed of metals, semiconductors, polymers, and ceramics, among other materials. Due to increased surface area and unique quantum effects, the characteristics of materials at this scale can differ dramatically from those at larger scales.

1.2.1. Classification of Nanomaterials

Nanomaterials can be categorized according to their dimensionality, or the number of dimensions in which they display nanoscale characteristics[20]. Dimensionally, there are four primary categories of nanomaterials:

(I)   0D Materials
(II)   1D Materials
(III)   2D Materials
(IV)   3D Materials

1.2.1.1. *Zero-dimensional materials*

Zero-dimensional (0-D) nanomaterials are nanoparticles with nano-scale sizes but no length, breath, or height. Quantum dots have unique electrical, optical, and magnetic capabilities due to their smaller size and effect of quantum confinement. 0-D nanomaterials include gold and silver nanoparticles[21].

1.2.1.2. *One-dimensional materials*

A one-dimensional (1-D) nanomaterial is a form of one dimensional extended material in nanoscale range and remaining dimensions in the micrometer range or greater[22]. 1-D nanomaterials including nanorods, nanowires and nanotubes etc. are being synthesized and used in different fields.

1.2.1.3. *Two-dimensional materials*

A two-dimensional (2-D) nanomaterial is a form of nanomaterial whose two dimensions are on the nanoscale scale, whereas the third dimension is often on the micrometer or greater scale. Due to low thickness and larger surface-volume ratio and these materials could be flat and thin[23]. 2-D materials such as TMDs, graphene and it's derivatives such as GO and rGO have been implanted in numerous applications.

1.2.1.4. Three-Dimensional Materials

The materials which have all dimensions in the nanoscale range known as the three dimensional (3D) nanomaterials[24]. These materials have a complicated, three-dimensional structure that can be porous or non-porous. This includes bulk powders, nanowire bundles, and a variety of nanotubes.
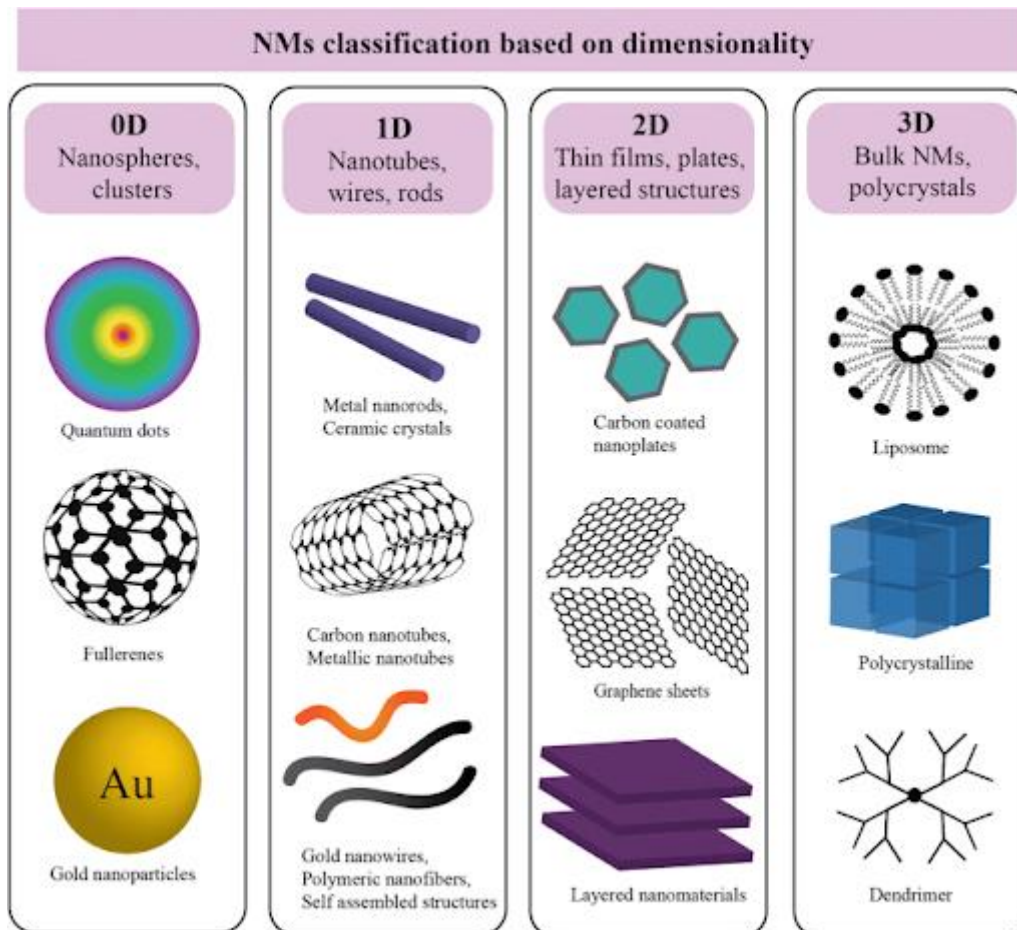
Figure 1.3: Representation of nanomaterials classifications[25].

1.3. Types of 2D Nanomaterials

There are different types of 2D Nanomaterials, some of which are includes:

- Transition metal dichalcogenides
- Graphene oxide
- Hexagonal boron nitride
- Silicene
- Silica glass
- Max phase

1.3.1. Graphene

Graphene has carbon atom arranged in hexagonal manner and make the 2D multilayer strcutre. It is very strong, flexible, and good at conducting electricity, heat, light weight and higher surface area. Graphene is being used in many different areas, like electronics, energy storage, and biomedical engineering. Further, graphene can be modified to change the functional, physical and chemical properties by oxidation and reduction of graphene.

1.3.2. Transition metal dichalcogenides

Transition metal dichalogenides (TMDs) is also a family of 2-D nanomaterials that are made up of layers of transition metal such as molybdenum or tungsten sandwiched between layers of chalcogen atoms such as sulfur or selenium[26]. TMDs possess exceptional electrical and optical properties, which position them favorable to utilized in field including like electronics, photocatalysis, and energy storage and conversion, amongst others.

1.3.3. Silicene

Silicene is a 2D substance consisting of silicon atoms organized in a hexagonal lattice, resembling graphene but with a weaker structure and has the same electrical properties as graphene[27]. They can also be used to make electronics circuits with silicon. Using vapor deposition, silicene was used to build a silicon layer one atom thick on the surface of a silver crystal. This layer was then used to make things like transistors and photodetectors, which are electronic devices.

1.3.4. Hexagonal boron nitride

A 2D substance with a similar structure to graphene but composed of boron and nitrogen atoms rather than carbon atoms[28]. Utilized in electrical and optoelectronic devices because it potential chemical stability, higher thermal conductivity and suitable insulating properties.

1.3.5. Silica glass

Silica glass, which is also known as fused quartz or fused silica has a porous struccture and it is the amorphous form of silica (SiO_2) created by melting crystalline silica at a very high temperature and then cooling it to prevent crystallization. Silica glass is renowned for its extraordinary optical qualities, which include great transparency and little thermal expansion, high resistance to heat, and chemical corrosion. It has a very high melting point (about 1,700 °C) and excellent thermal and chemical resilience[28].

1.3.6. Max phase

Excellent physiochemical properties of 2D materials including graphene have much attracted the interest of researchers. The MAX phase is made up of many crystals (polycrystalline). They are both electrically and thermally conductive, and they stay stiff at high temperatures and keep their rigidity and stiffness[29].

The MAX program has more than 100 phases[30]. The formula for MAX in its most generic form is $\mathbf{M_{n+1}AX_n}$, where;

$\mathbf{n}$ = 1,2, or 3 (M_2AX, M_3AX_2, or M_4AX_3 etc.)	$\mathbf{A}$ = group IIIA and IVA like Al, Si, Ga elements
$\mathbf{M}$ = transition metal like Ti, Nb, V, Mo, W andTa	$\mathbf{X}$ = carbon (Carbides), Nitrogen Nitrides or both Carbonitrides C/N

The bonding between M and A is metallic bonding. Typically, the A atoms are placed in a layered structure with a hexagonal close-packed arrangement, and the metal atoms are situated between these layers. Generally, the metallic connection between metal atoms is greater than the metallic bonding between metal and A atoms[31]. The bonding between M and X are ionic, the X atoms are positioned at the corners of octahedra that surround the metal atoms, forming a structure similar to that of rock salt. In addition, covalent bonds exist between the metal and X atoms due to the partial sharing of electrons. The covalent bonding becomes increasingly prominent as the value of the Max phases increases.
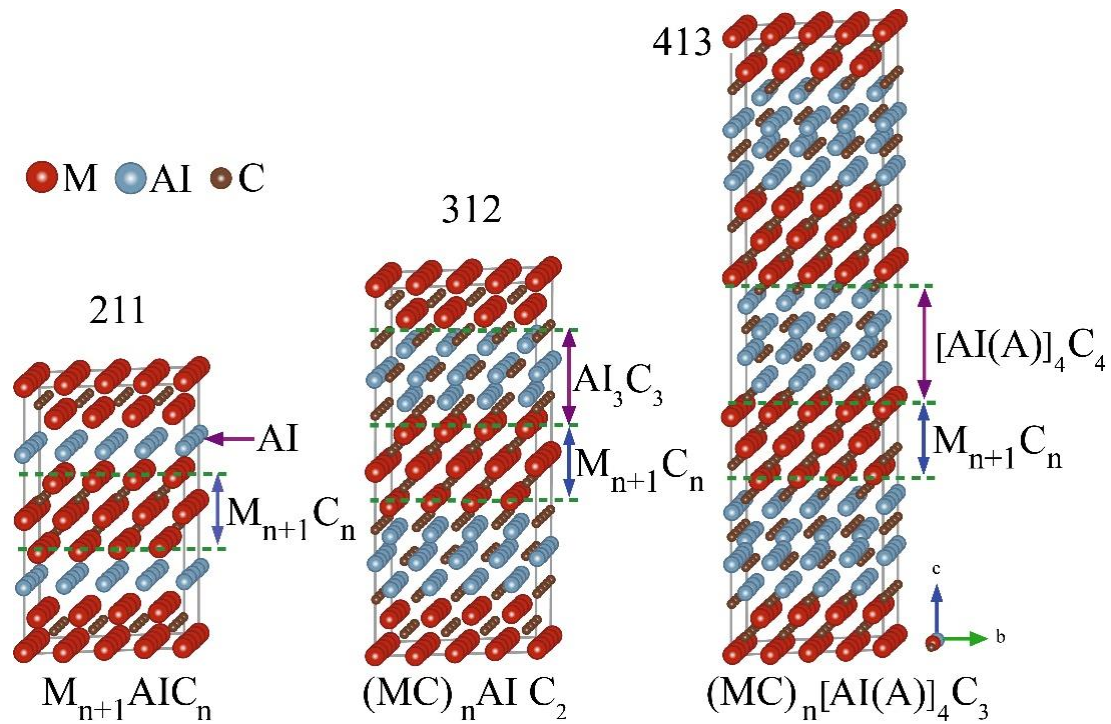
Figure 1.4: MAX-phase unit cell structure of 211 (n=1), 312 (n=2) and 413 (n=3) Reproduced with permission from reference[32].

1.4. MXene

The M in MXene represents a transition metal, and the A represents "A group" metal. In 2011, a new member of the family of two-dimensional metal carbides, carbonitrides, and nitrides were identified. There are around thirty distinct MXene variants produced through experimentation[33]. MXene is represented by the formula $\mathbf{M_{n+1}X_nT_x}$.

$\mathbf{n}$ = 1, 2 or 3 $\mathbf{X}$ = carbon, nitrogen,

$\mathbf{M}$ = transition metal $\mathbf{T}$ = surface terminations (OH, or F).

Crystalline MXene can have a variety of different structures, depending on the particular composition as well as the synthesis process. However, many MXene has a crystal structure known as hexagonally close-packed (HCP)[34]. This implies that the metal atoms are grouped in a hexagonal arrangement. Atoms "M" are organized in a hexagonal manner and atoms "X" fill voids in octahedral structure.
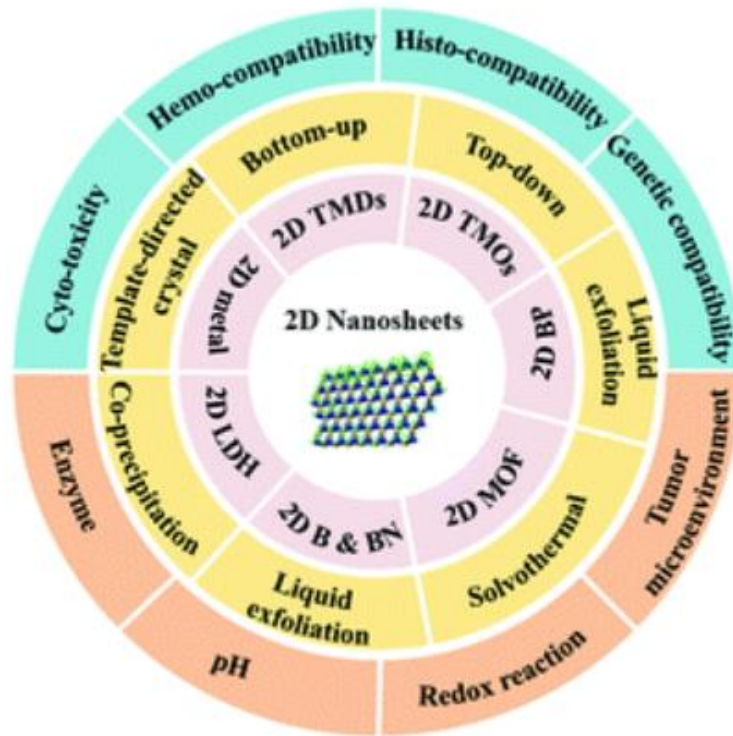
Figure 1.5: Representation of 2D Nanostructure[35].

1.4.1. Synthesis of 2D MXene

In order to synthesize 2D MXenes, it is usually required to etch the A element selectively which is commonly aluminum from MAX phases which is either ternary carbides or nitrides[36]. This etching procedure can be accomplished using a variety of techniques, such as etching with hydrofluoric acid (HF) or electrochemical etching, for instance. The material is washed and exfoliated in order to obtain individual sheets of MXene.

The first MXene was found in 2011, named Ti_3C_2Tx. It was made by eliminating the A layer selectively from the Ti_3AlC_2 MAX phase in HF. Since that time, HF has been widely accepted as a primary etchant for MAX phases that contain an Al layer.

1.4.2. Chemical synthesis reaction

The following pattern of three reactions determines the exfoliation and removal of A layers during the chemical reaction.

$$M_{n+1}AX_n + 3HF = M_{n+1}X_n + AF_3 + 3/2\ H_2 \quad ...\ldots\ldots\ldots\ldots\ldots(1)$$

$$M_{n+1}X_n + 2\ H_2O = M_{n+1}X_n\ (OH)_2 + H_2 \quad \ldots\ldots\ldots\ldots\ldots(2)$$

$$M_{n+1}X_n + 2HF = M_{n+1}X_nF_2 + H_2 \quad \ldots\ldots\ldots\ldots\ldots(3)$$
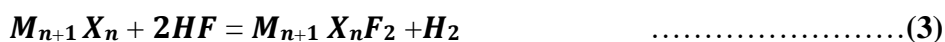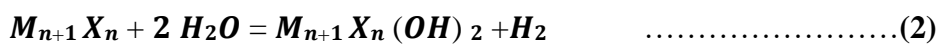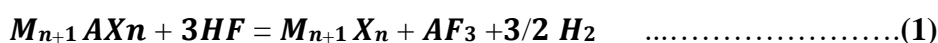
Reaction 1 is regarded as the basic step in the etching process, equations (2) and (3) are processed simultaneously. H_2 gas is produced during etching and bubbles appear in the container when MAX powder is added. Etching in an aqueous solution produces MXene particles with functionalized surfaces. These terminations may be -O, -OH, -F, -Cl, or -S depending on the etchant material utilized. After the completion of etching process, the multilayered product of MXene can be acquired by washing the solution numerous times with deionized water until all the acid is completely removed. To obtain a few layers to a single layer of MXene, the obtained multilayered MXene is processed through delamination or intercalation. The etching and washing process replaces the M-A stronger bonds with weaker bonds (hydrogen) and Van der Waals forces make the multilayered MXene easily delaminated. However, it's important to note that the M-X bond remains significantly stronger (about 6-8 times) than the bond in graphite. Therefore, scotching exfoliation of multilayered MXene will not result in the formation of monolayers After successful etching, the characteristic peaks of MAX phase in XRD vanish, leaving only the peaks related to the basal planes of MXene ($M_{n+1}X_nTx$) layers which appear broadened and shifted towards a lower angle. In (0002) plane, the bulk of MXenes exhibit significant downshifting and widening.

In many instances, the current methods for etching do not completely eliminate the A layers, leading to impurity peaks alongside the characteristic MXene peaks. However, post-processing techniques, such as delamination, intercalation, and repeated centrifugation, can be used to isolate partially etched MXene from unreacted MAX impurities. These techniques will be comprehensively explained in the next chapter. The layers comprising $M_{n+1}X_n$ are held together by Van der Waals bonding, which is relatively weak. These layers can be separated using sonication, but this technique tends to yield flakes that are both thin and electron-transparent, and that have a relatively low concentration.
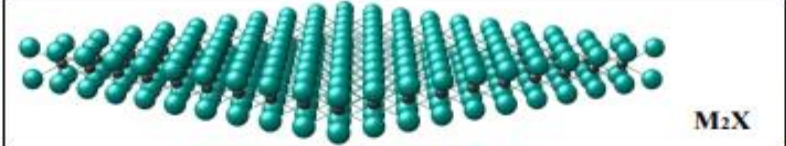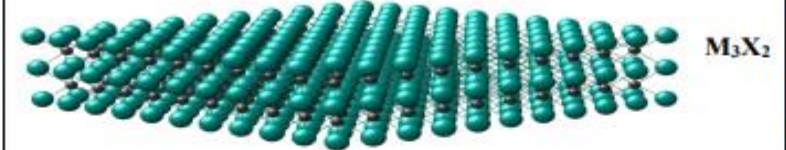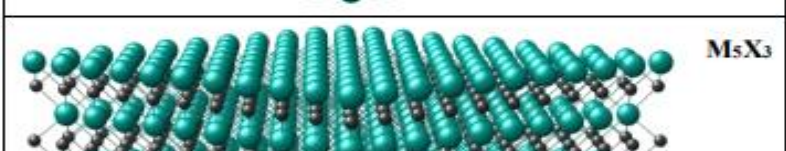
Figure 1.6: Representation of few well-known MXenes and their structure [Zahra et al].

1.5. Application of nanomaterials and nanotechnology

Nanomaterials have changed the way we think about materials science and engineering. These nanometer-sized particles have unique characteristics that differ from those of bulk materials. Nanomaterials have several uses in medical, electronics, energy, and materials research. They can make stronger, lighter, and more durable materials, enhance energy production and storage, and even eliminate contaminants from the environment. Nanomaterials can be used in medicine to deliver medications to specific cells or tissues, and in electronics to make smaller, more efficient devices. Nanomaterials are an intriguing

and fast-increasing topic of study with many possible applications due to their variety and innovation potential.

Figure 1.7: Application of nanomaterials and nanotechnology[37].

1.5.1. Energy storage

Due to their unique features and potential for innovation, nanomaterials have gained significant importance in energy storage applications. These nanomaterials have vast surface areas, superior electrical conductivity and the capability to rapidly store and release significant quantities of energy. Nanomaterials such as graphene, carbon nanotubes, and metal oxides were used to increase the energy density and charging rate of supercapacitors. Additionally, nanomaterials were utilized in solar cells to enhance energy storage and hydrogen storage for fuel cell applications.

Figure 1.8: Representation of nanomaterials applications in energy storage[38].

1.5.2. Electronics

Nanomaterials have revolutionized the field of electronics with exceptional properties and potential in other applications. The use of nanomaterials in electronics has shown the major out such as in flexible nano based biosensor and wearable electronics. Nanomaterials have been employed in the manufacturing of high-performance transistors, memory devices, and sensors. In addition, they provide enhanced electrical conductivity, enabling the development of highly efficient and durable electrical devices. Furthermore, nanomaterials' tiny size makes them suitable for usage in downsized electronic components and integrated circuits, resulting in smaller and more compact devices. Nanomaterials have the capability to stimulate the performance of solar cells, allowing for a more effective method of solar energy harvesting. Nanomaterials have great potential for electronics and will likely continue to drive innovation in the industry.

1.5.3. Batteries

Nanomaterials have emerged as a viable way to enhance the performance and efficiency of batteries. The high surface area to volume ratio of nanomaterials, which improves the electrode-electrolyte interface and enables faster charging and discharging rates, is one of the primary benefits of employing nanomaterials in batteries. Nanomaterials including metal oxide nanomaterials, carbon nanotubes and graphene-based materials can be employed to enhance battery capacity, cycle life, and stability. Nanomaterials can also reduce battery size and weight, making them suitable for smartphones, laptops, and wearables. In addition,

13

the use of nanomaterials into battery systems can improve their safety by minimizing the risk of overheating and explosions.

1.5.4. Water treatment and purification

Nanomaterials' unique features like high reactivity, selective adsorption, catalytic activity and self-cleaning have made them popular in water treatment and purification. Heavy metals, chemical compounds, and pathogens can be removed from water sources using nanomaterials. Iron, aluminum, and titanium oxide nanoparticles, for instance, have been employed to remove arsenic, fluoride, and other impurities including bacteria and viruses from water. Nanomaterials can also disinfect by generating reactive oxygen species that destroy bacterial cell walls and inactivate viruses. Nanomaterials in water treatment and purification can improve water quality and provide safe drinking water to the world.

Chapter 02: Literature Review

In this chapter, we will be providing an introduction to MAX and MXene. The many different techniques for etching to convert the MAX phase to MXene and theoretical discussions about the structure of MXene, which include surface termination attachments, are presented here. Also, a brief literature overview regarding the application of MXene in water-splitting application is as follows.

2.1.   Importance of 2D Materials

Two-dimensional materials, often known as 2D materials[31,39], are an interesting family of materials because of their distinctive electrical, optical, and mechanical characteristics and even biomedical devices. Some examples of 2D materials are graphene, graphene oxide (GO), reduced graphene oxide (rGO), hexagonal boron nitride (hNB) and transition metal dichalcogenides (TMDS). These materials have a thickness of only one or a few atomic layers, which makes them incredibly thin, flexible and transparent. Moreover, they have a high surface-to-volume ratio. The ability to regulate their properties at the atomic scale gives a significant opportunity for improvement in technologies like energy conversion and storage, sensing, electronics, optoelectronics and catalysis. Its low dimensionality and huge surface area allow them to investigate fundamental physical and chemical processes, advancing basic science and practical applications.

2.2.   Max Phase

The MAX phases are a category of materials that have been characterized by their unusual combination of metallic and ceramic properties. early transition metal "M" and the elements from group IIIA or IVA represented "A" and X is either carbon or nitrogen that makes up their structure. The name "MAX" comes from the first letters of each element in the formula.

The commonly used formula for Max is $M_{n+1}AX_n$, (MAX), Where n is 1,2,3.

In the 1960s, Nowotny et al. discovered the highest number of MAX Phases in powder form to date. Barsoum and his team accidentally found the first Max phase (more than 70 different compositions of Max phase have been identified), Ti_3SiC_2, while exploring titanium silicon carbide ceramics. They observed that the material comprised alternating layers of titanium and silicon carbide, like graphite. This encouraged them to search for further Max phases, which they found in Ti_2AlC, Ti_3AlC2, and Ti_4AlN_3.

 'M' and 'A' components of the MAX Phases are listed in Tables 1 and 2.

Table 2.1: List of early transition metals

Elements	Name	Atomic number
Sc	Scandium	21
Ti	Titanium	22
V	Vanadium	23
Cr	Chromium	24
Zr	Zirconium	40
Nb	Niobium	41
Mo	Molybdenum	42
Hf	Hafnium	72
Ta	Titanium	73
W	Tungsten	74

Table 2.2: Elements of group A in the periodic table

Elements	Name	Atomic number
Al	Aluminum	13
Si	Silicon	14
P	Phosphorous	15
S	Sulfur	16
Ga	Gallium	31
Ge	Germanium	32
As	Arsenic	33
Cd	Cadmium	48
In	Indium	49
Tl	Thallium	81
Pb	Lead	82

MAX phases have a graphite-like layered crystal structure[40]. Its structure offers them tremendous strength, stiffness, and thermal shock resistance. They also have outstanding electrical and thermal conductivity, making them appropriate for a variety of industrial

applications. MAX phases are diverse due to their capacity to replace or add components to the crystal structure and utilize a variety of transition metals and group IIIA or IVA elements. MAX phases are tailored for specific applications such as wear-resistant coatings, cutting tools, and high-temperature structural materials.

Table 2.3: Summary of MAX phases

413 MAX Phases	312 MAX Phases	211 MAX Phases
Ti_4AlN_3	Ti_3AlC_2	Ti_2CdC, Nb_2SnC, Nb_2PC, Mo_2GaC, Zr_2TlN,
V_4AlC_3	V_3AlC_2	Zr_2SnC, Nb_2AsC, Zr_2SC, Nb_2SC, Hf_2TlC,
Ti_4GaC_3	Ti_3SiC_2	Ta_2AlC, Ta_2GaC, Hf_2PbC, Hf_2SnN, Sc_2InC, ,
Ti_4SiC_3	Ti_3GeC_2	Ti_2SC, Zr_2InC, Zr_2PbC, Ti_2GaC, Tl_2InC,
Ti_4GeC_3	Ti_3SnC_2	Ti_2TlC, V_2AlC, Cr_2GaC, Ti_2AlN,Ti_2InN,
Nb_4AlC_3	Ta_3AlC_2	V_2GaC,V_2GaN,Hf_2SnC,Cr_2GaN, Ti_2PbC,
Ta_4AlC_3		V_2GeC, Cr_2AlC, Cr_2GeC, Ti_2GeC, Ti_2SnC,
		V_2PC, Zr_2TlC, Nb_2AlC, Nb_2GaC, Nb_2InC,
		V_2AsC,Hf_2SC

2.3. MXene

The primary idea of this thesis is associated with MXene. The above information and facts are written primarily to introduce the topic of unique 2D materials, MXene. MXenes are a class of 2-D nanomaterials generally derived from MAX Phases using different etching techniques. By using a wet chemical reduction process on the middle "A" layer and finally getting hexagonally stacked sheets of "MX" layers, MXenes are obtained from its 3D parent Phase known as "MAX." 3, 5, or 7 atomic layers contribute the final MXene sheets for M_2X, M_3X_2, and M_4X_3. Ti_3C_2Tx, Ti_2CTx, V_2CTx, Nb_2CTx and Mo_2CTx are all examples of MXene. Researchers are studying this newly found 2D material in addition to other MXene phases.

2.3.1. Synthesis of MXene

MXene is composed of transition metal carbides, nitrides, or carbonitrides which have been considered 2-D nanomaterials. Synthesis of 2D MXene typically involves the etching of the "A" element selectively from MAX phase material using fluoride ions, followed by delamination and exfoliation to obtain individual MXene layers.

One commonly used method for synthesizing 2D MXenes is the HF etching method, which involves immersing the MAX phase precursor in an HF-containing solution. The HF reacts with the aluminum (A) layers, causing them to dissolve and leaving behind the 2D MXene layers. The resulting MXene layers can then be washed and delaminated to obtain individual 2D sheets.

2.3.2. Synthesis factors

The synthesis of materials, including 2D MXenes, can be influenced by a variety of factors. Here are some of the key factors that can affect the synthesis of 2D MXenes[41]:

- Etching time
- Etching method
- Particle size of respective MAX phase powder
- Etching temperature
- Concentration of HF

Overall, the various factors involved in the synthesis of 2D MXenes are interconnected, and optimizing such factors could lead in the improvements of reaction rate, completeness, and properties of the resulting MXene material.

2.3.3. Different etching routes

In 2011 at Drexel University, MXene materials were discovered and since then various etching routes have been developed and refined for the synthesis of these materials. Here is a brief history of the development of different etching routes for MXene synthesis:

2.3.4. Acid etching

Acid etching is the most frequently used for etching MXene and synthesis, and it was first reported in 2011. They used a mixture of hydrofluoric acid and hydrochloric acid to particularly remove the "A" layer from the precursor of MAX phase and prepared first MXene material Ti_3C_2Tx.

2.4. Separation of Single Layer Flakes from Multilayered MXene

Delamination process in which single-layer flakes seprate out from multilayered MXene involves the selective removal of the intercalated species that hold the layers together[42]. This separation of flakes is crucial for exploring the full potential of MXenes for numerous applications includinh energy storage and conversion devices. Similar to other 2D materials,

research shows that converting multilayer MXene to single or a few layers considerably improves its electrochemical performance. Most of materials which has 2D structure has in-plane strong bonding and Van der Waals weak bonding at the outer layer are divided into monolayers using scotch sellotape. So far, as mentioned previously in this chapter, MXene has a special M-X bonding that prevents mechanical exfoliation.
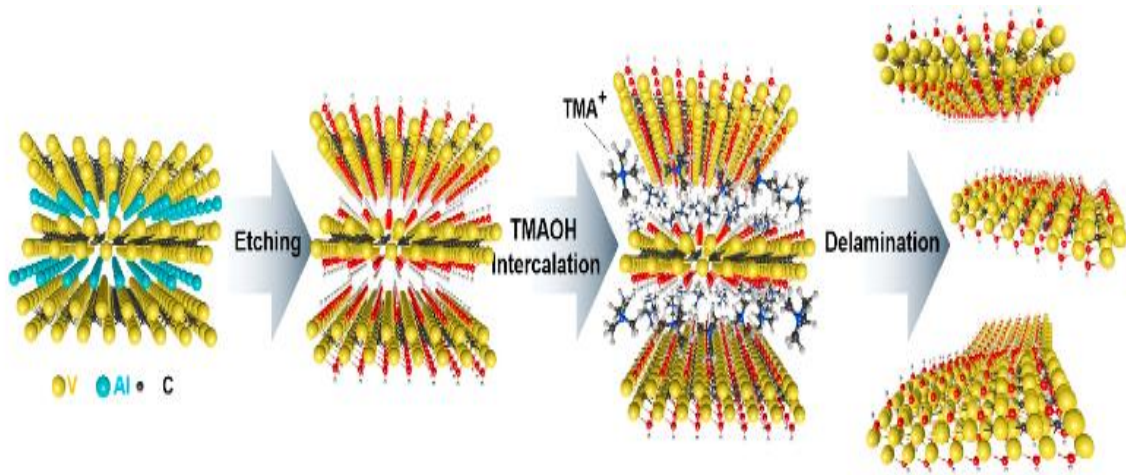
Figure 2.1: MXene delamination and wet chemical etching[43].

Large-scale production for industrial purposes is not possible with liquid phase exfoliation due to its limited scalability. Multilayered MXene particles can be separated from single/few-layer flakes, however this requires additional processes or post-processing of etched particles and is therefore not a straightforward method. Delamination frequently weakens interlayer forces and increases their distance. To do this, typically large organic/inorganic molecules are intercalated between the layers. The addition and processing of larger molecules results in an expansion of layers and a reduction in the contact between $M_{n+1}X_n$ layers, followed by the MXene layers swelling due to the water molecules and ions co-intercalation. The addition and processing of larger molecules results in an expansion of layers and a reduction in the contact between $M_{n+1}X_n$ layers, followed by the swelling of MXene layers due to the co-intercalation of water molecules and ions. The proper intercalant and optimal techniques reduce delamination energy barrier, resulting in single/few-layer MXene after sonication[44].

2.5. Properties of MXene

MXene is a relatively new category of 2-D materials that has been received a considerable attraction by researchers in previous decade because of its unusual characteristics and

prospective applications[45]. The following is a list of some of the properties that MXene possesses:

2.5.1. Good electrical conductivity

MXenes have a high electrical conductivity makes them intriguing candidates as materials for use in electronic devices and applications involving energy storage.

2.5.2. High surface area

MXenes have a high surface area that makes them appealing for use in applications like catalysis, gas detection, and water purification because of their huge surface area.

2.5.3. Good mechanical properties

Excellent mechanical properties MXenes have good mechanical properties, including a high strength and toughness, which makes them suitable for applications such as flexible electronics and structural materials. These properties also make MXenes more environmentally friendly.

2.5.4. High thermal stability

MXenes are thermally stable up to very high temperatures that marks them desirable for use in high temperature applications including thermal management because of their high level of thermal stability.

2.5.5. Tunable surface chemistry

The surface chemistry of MXenes may be modified by altering the composition and surface functionalization, these materials are versatile and could be utilized for a wide variety of applications.

2.5.6. Biocompatibility

Some MXenes have been found to be biocompatible, which makes them attractive for biomedical applications such as drug delivery and biosensors.

In general, MXenes are promising materials for a vast array of applications due to their exceptional combination of characteristics.

2.6. Application of MXene

The MXene family is growing rapidly as a result of advances in synthesis techniques leading to a extensive range of new hybrid nanocomposite and applications. MXenes are viewed as multifunctional materials due to their adaptable and large surface area, adsorption

capabilities (which vary with termination group), highly reactive surface, and many other features[46]. Several applications of MXene are in severe need of modern demands and are described below:

2.6.1. Catalytic Activity

Owing to their catalytic properties, MXenes are commonly utilised as functionals for oxidizing CO and in water-splitting reactions to produce hydrogen. CO oxidation is a significant aspect since it aids in the solution to the problem associated with cars and industrial waste. There will always be a demand for the catalyst that satisfies both efficiency and cost requirements[47]. The MXene catalyst displays exceptional efficiency at a low potential range of 30 and 77 mV, achieving currents of 10 $mAcm^{-2}$ and 100 $mAcm^{-2}$, respectively. Also, Mxene has shown 40 times higher mass activity as compared to the commercially available platinum on carbon based catalyst.

2.6.2. Electrolysis of water

Electrolysis is a process that involves passing an electric charge through an electrolyte, resulting in redox reactions. The entire reaction of the water can be seen in the following chemical equation[48].

$$4OH^- \rightarrow O2 + 2H2O + 4e^-$$ (At Anode)   …… (2.1)

$$4H2O + 4e^- \rightarrow 2H2 + 4OH^-$$ (At Cathode)   ……..(2.2)

$$2H2O + Electricity \rightarrow O2 + 2H2$$ (Overall reaction)   ………(2.3)
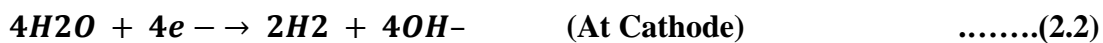
The energy required for this process can come from various sources, including renewable or non-renewable energy sources. By using electrochemical water-splitting tools, hydrogen can be generated using sources of renewable energy like wind turbines which can stored the efficient energy with clean environmentally manner. This is particularly important since hydrogen is a clean fuel that does not emit greenhouse gases when combusted, making it a cleaner method of hydrogen production compared to conventional methods such as natural gas and coal.

In oxygen evolution reaction, the water splitting reaction efficiency could be affected due to large anodic overpotential which can impede the hydrogen evolution reaction and it reduce the splitting reaction rate. To design the effective oxygen evolution reaction catalyst for water splitting then it is compulsory to understand the mechanism of thermodynamics and kinetics of reactions. The electrocatalytic process for water splitting composed of two

half cell reactions and water electrolysis is the primary process in a fuel cell. The most commonly used method in industries is alkaline water electrolysis[49]. This research project focuses on alkaline water splitting, which is more relevant to industrial applications. The processes of the two primary water-splitting reactions such as the oxygen evolution reaction (OER) and the hydrogen evolution reaction (HER) has been discussed in the following sections.
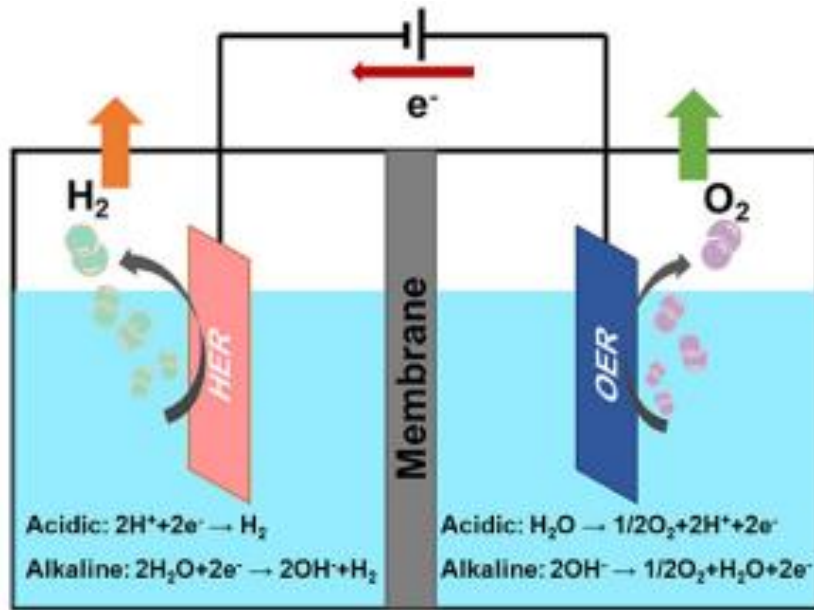
Figure 2.2: Representation of water splitting phases.

2.6.3. Overpotential

One of the most common ways of measuring the effectiveness of an electrocatalyst is by assessing its ability to generate high current densities at the lowest possible overpotential[50]. Overpotential is the excess voltage needed to drive the electrode to a specific rate:

$$\eta \; = \; Ee - Et \qquad .... \; (2.4)$$

In above equation, Ee and Et represents the applied potential and thermodynamic potential respectively and the overpotential is denoted by η. Although appropriate selection of these parameters can reduce overpotential, it cannot be entirely eliminated, but only minimized. In OER, a desirable overpotential range is typically between 300-400 mV, indicating effective catalyst performance. However, it is rare to find catalysts with overpotentials below 300 mV.

2.6.4. Tafel slope

The Tafel slope helps to demonstrate the performance of a catalyst and it is a crucial parameter which provide the insights into the fundamental kinetics of the reaction[51]. The enhancement in overpotential is help to achieve a particular current density.

The Butler-Volmer limiting case equation:

$$j = j0[exp\,(\alpha az F\eta/RT\,) - exp\,(-\alpha cz F\eta/RT)] \qquad \text{......... (2.5)}$$

It used to derive the Tafel equation and jo represents the exchange current density which is a key parameter to describes forward and reverse reactions rate at equilibrium potential. Tafel slope (b) is calculated as b = 2.303RT/αF, where a is a constant and the anode and cathode charge transfer coefficients are aa and ac respectively, where j is the current density, η is the overpotential, z is the number of electrons transferred in the reaction, F is Faraday's constant, and R is the universal gas constant. A higher Tafel slope indicates that the overpotential increases more rapidly with current density. To achieve high current densities at lower overpotentials in an electrochemical process, a catalyst with a lower Tafel slope is required.

2.6.5. Electrolyte

The type of electrolyte that used could have a significant effect on performing of OER catalyst in water splitting application. In an alkaline environment, the OER process would be beneficial as it ensures the stability of the catalyst. Conversely, the stability of the catalytic material in OER could decrease in neutral and even more in acidic pH solution. This could be due to the high oxidative potential of OER at pH = 0 that can cause the electrode to corrode. To maintain steady catalytic functioning, OER is often carried out in an alkaline environment[52]. However, researchers are still working on developing an OER catalyst that can perform consistently under all pH regimes. This challenge requires further exploration and investigation by electrochemists.

2.7. Electrochemical Water-Splitting application using V_2CTx Composites

Park, S., et al. 2022, This research focuses on modifying the electronic structure of V2CTx MXene by introducing atomic substitutions of Pt atoms in order to enhance the catalytic activity of Pt–V_2CTx towards the hydrogen evolution reaction (HER). The goal is to reduce the binding force of hydrogen on V_2CTx through the confinement of Pt atoms, thereby

promoting improved catalytic performance. Specifically, the study investigates the Pt–V_2CTx catalyst's behavior in acidic media, where it exhibits 27 mV overpotential at a current density of 10 mA/cm^2 and highlight excellent catalytic potential[53].

Zahra, S.A. et al. 2022, In this study, a material design approach was employed to enhance the properties of V_2CTx MXene sheets by incorporating multi-walled carbon nanotubes (MWCNTs) onto their surfaces, resulting in a hybrid structure known as MWCNT@V_2CTx. The MWCNTs catalyst exhibited remarkable durability, as demonstrated by the chronoamperometry test conducted over a period of 16 hours. At 10 mA/cm^2 current density demonstrated excellent performance with minimal overpotentials of 27 mV for the hydrogen evolution reaction (HER) and 469 mV for the oxygen evolution reaction (OER) for hybrid catalyst. These results highlight the enhancement of electrocatalytic properties of the MWCNT@V_2CTx hybrid catalyst[54].

Yang, L., et al. 2022, Via the hydrothermal method, fabricated a self-sustained electrode by combining Iron Nickel LDH, V_2CTx MXene and a nanofiber substrate (NF) for OER and HER. The strong interfacial interaction within the nanocomposite created numerous active sites, resulting in enhanced electrical conductivity and mechanical stability. When evaluated in 1M KOH, the electrocatalyst (FeNi LDH/V_2CTx/NF) exhibited excellent performance with 222 mV and 151 mV overpotential y at a current density of 10 mA cm^{-2} for OER and HER respectively[55].

Wang, J.et al. 2022, employed a simple deposition method to uniformly anchor Platinum nanoparticles onto the surfaces of 2D V_2CTx MXene, resulting in the formation of a Pt/V_2CTx nanocomposite. The catalysts obtained, Pt/V_2CTx, exhibited excellent performance in 0.5M H_2SO_4 electrolyte, with a lower Tafel slope of 20.6 mVdec^{-1} and an overpotential of 67 mV[56].

2.8. Electrochemical water-splitting application of Ti_3C_2Tx and composites

Jianxing Wang et al. 2018, Co-Ti_3C_2Tx hybrid electrode material was successfully engineered for efficient HER in alkaline media. The obtained results demonstrated an impressive performance with an overpotential of -300 mV and a Tafel slope of 147 mV/dec in a 1 M KOH solution. This hybrid electrode exhibited a larger electrochemical surface area, increased roughness factors, high capacitance values, and reduced overpotential, highlighting its potential for enhanced electrochemical reactions.[57]

Lan Huang et al. 2019, reported the heterogeneous composite by in situ growth of MoS_2 nanosheets vertically on Planar Ti_3C_2Tx nanosheet (MoS_2/Ti_3C_2Tx) using aqueous technique. This unique configuration exhibited 280 mV remarkable overpotential at 10 $mAcm^{-2}$ current density which accompanied by Tafel slope of 68 mV dec^{-1} which relatively and excellent stability in 0.5 M H_2SO_4 for 36 hours. This study considerably contributes to our understanding of developing water splitting electrocatalysts based on Ti_3C_2Tx MXenes[58].

Iffat A., et al. 2021, reported that $Ti_3C_2Tx@MoO_3$ and Ti_3C_2Tx MXene both exhibited distinct performance OER characteristics. $Ti_3C_2Tx@MoO_3$ demonstrated 190mV overpotential and 59mV dec^{-1} Tafel slope. But, Ti_3C_2Tx MXene exhibited an overpotential of 450mV overpotential with 89mV dec^{-1} Tafel slope[59].

Chapter 03: Experimentation

This chapter provides a brief overview of equipment used during the experimental synthesis of MXene and their composites, specifically Ti_3C_2Tx and V_2CTx, as well as the methods used to synthesize composites for electrode fabrication and electrochemical analysis. Additionally, various characterization techniques including XRD, SEM, EDX, Raman, FTIR and LSV are discussed in detail for analyzing the structural, elemental, and electrochemical properties of the materials.

3.1. Synthesis method

Two fundamental approaches have been employed to synthesize the nanomaterials such as: top-down and bottom-up approaches.

The first is a bottom-up method can synthesized the high-quality 2D nanomaterials on a variety of substrates and in this approach mostly chemical vapor deposition (CVD) technique has been used. But, MXene could not synthesized using this approach because the resulting films are very thin and not monolayer or single layer.

For our study, we chose the top-down route to synthesize Vanadium-based MXene from MAX Phase. This approach allows us to reach the nanoscale and create a nanocomposite with a large surface area, better electronic properties, and an enhanced density of states. We selected Vanadium-based MXene as the first precursor, which can be considered as a matrix in a nanocomposite scenario.

A representation of the reaction is as follows:

$$Mn + 1AXn \; + \; 3HF \; = \; Mn + 1\,Xn(s) + \; AF3 \; + \; 1.5H2\,(g) \qquad \ldots\ldots\ldots\ldots..(3.1)$$

$$Mn + 1Xn(s) \; + \; 2HF \; = \; Mn + 1XnF2 \; + \; H2\,(g) \qquad\qquad \ldots\ldots\ldots\ldots..(3.2)$$
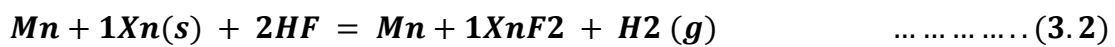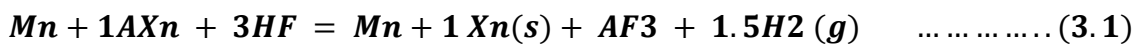
3.2. Synthesis of materials

Several chemicals and methods are required for the synthesis of desired substances. The necessary ingredients (materials and chemicals), equipment, and steps for the preparation of MXene and Erbium-decorated MXene are listed below.

3.2.1. Chemicals and Apparatus

Table 3.1: List of equipment that was used during synthesis.

• Weight balance	• Petri dish

• **Teflon autoclave**	• Half-face protection mask
• **Hotplate**	• Gloves
• **Vacuum drying oven**	• Safety goggles
• **pH test strips**	• Filter paper (0.2μm)
• **Magnetic Stirrer**	• pH paper
• **Centrifuge tubes**	• sonicator
• **Centrifuge machine**	• Beaker
• **Vacuum filtration assembly**	• Lab Spatula

3.2.2. Chemicals

The chemicals presented in Table 5 were utilized in the process of synthesizing MAX, MXene, their derivatives, as well as for electrochemical testing.

Table 3.2: Provides a summary of the chemicals employed for synthesizing MAX, MXene, composites and electrolytes.

Chemical name	Formula	Source
MAX Precursor (Vanadium Aluminum Carbide, Titanium silicon carbide)	V_2AlC, Ti_3SiC_2 [300 Mesh Size, 95% pure]	Sigma Aldrich
Hydrofluoric acid (49 wt. % in H2O, ≥99.99%)	HF	Sigma Aldrich
TMAOH (Trimethyl ammonium hydroxide 25% w/w aqueous solution)	$(CH_3)_3NOH$	Sigma Aldrich
Potassium Hydroxide	KOH	Sigma Aldrich
N-Methyl-2-pyrrolidinone (NMP)	C_5H_9NO	Sigma Aldrich
Absolute Ethanol	C_2H_5OH	Sigma Aldrich
Acetone	C_3H_6O	Sigma Aldrich
Polyvinylidene fluoride (PVDF)	$-(C_2H_2F_2)n-$	Polyvinylidene fluoride

Nafion (Binder)	$C_7HF_{13}O_5S.C_2F_4$	Sigma Aldrich
Deionized Water	H_2O	Sigma Aldrich
Hydrogen per Oxide	(H_2O_2) (25 wt. % in H_2O, ≥99.99%)	Sigma Aldrich
Erbium nitrate hexahydrate	$(Er\,(NO_3)_3._6H20)$	Sigma Aldrich
3.3. MXene Synthesis		

3.3.1. Synthesis of Ti₃C₂Tx MXene

To prepare the etching mixture of MXene, a combination mixture of hydrogen peroxide and hydrofluoric acid with 5 mL and 45 mL respectively was added to a Teflon beaker. The Mixture was kept in an ice bath under continuous stirring for 30 min then added 3 g powder of Ti_3SiC_2 MAX. To ensure the temperature remained at or below 5 °C during the exothermic etching process, the beaker's lid was kept loose to allow the release of hydrogen gas. The solution was transferred to pre-heated oil bath at 30 °C and placed continuous etching for 46 hours. Then, stopped the etching process.

For washing of the MXene, 5 cycles were performed, each involving the addition of 45 mL of deionized water to a centrifuge tube containing the Ti_3C_2 MXene sludge. After each cycle of centrifuge, the supernatant water-like was separate out and added 50 mL of deionized water and kept continue the washing process. After 5th cycle, vacuum-assisted filtration was used to wash the Ti_3C_2 MXene flakes with 50 mL of deionized water, followed by adding more 100 mL deionized water. Finally, the Ti_3C_2 MXene flakes were seprated and dried in vacuum oven at 80 °C for 24 hours. It is important to note that the temperature of the ice and oil bath as well as the washing process were carefully controlled to ensure the purity and quality of the MXene flakes.

3.3.1.1. Delamination

To treat 1g of Ti_3C_2 powder, 2 mL of tetramethylammonium hydroxide (TMAOH) was added and manually shaken for 3 min that gave the wet MXene powder into a darker black color. In mixture, added 20 mL of deionized water to the mixture and kept for stirring at 300 rpm for 24 hours. Then, MXene sample was put for washing with DI water using centrifugation and repeat the washing process for five times. The washing cycles involved

6-minute cycles for the first three rounds and 10-minute cycles for the last two rounds at 3500 rpm.

The dilute green solution of Ti_3C_2 MXene appeared resilient after the 1st washing cycle. The pH of Ti_3C_2 basic solution became neutral after the 5th washing cycle. Vacuum-assisted filtration was used to further wash the MXene, resulting in freestanding MXene films. The MXene was collected from both processes after vacuum drying at room temperature for 15 hours and then again dried at 120 °C in vacuum oven.
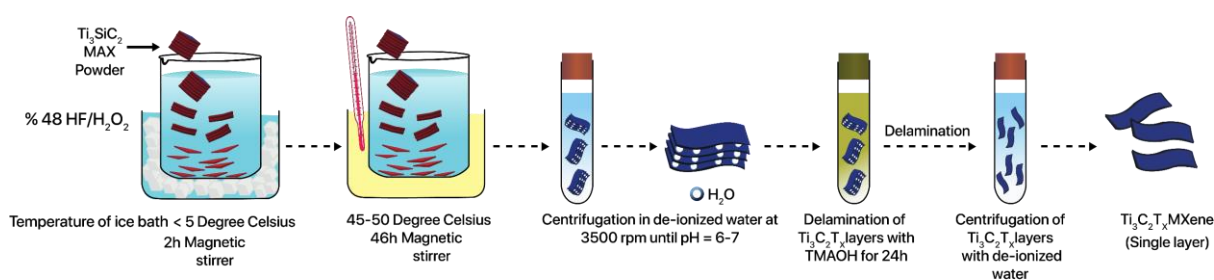
Figure 3.1: Synthesis process of Ti_3C_2Tx (Etching & Delamination).

3.3.2. Synthesis of V_2CTx

Two-dimensional materials were fabricated by etching the layers of Al from the precursor solution of V_2AlC. The synthesis process involved adding 20 mL of 49% of Hydrofluoric acid (HF) solution into a Teflon beaker fitted out using a bar magnetic stirring and placed the Teflon bath at room temperature (RT) and rotation speed to 200 rpm as per convenience to avoid the splashes. Next, 1 g powder of V_2AlC was gradually added to the reactor in batches over approximately 15 minutes as the reaction is highly exothermic, followed by closing the Teflon lid. Then, the mixture was kept under stirring for 96 hours at a constant room temperature, allowing the etching reaction to occur ($V2AlC + HF \rightarrow V2CTx + AlF3 + H2 \uparrow$). After 96 hours, the mixture was washed with deionized water using centrifugal speed of 6,000 rpm for 5 minutes. The centrifugation was stopped and filtered after a viscous precipitate emerged and PH reached at 6 or neutral. The resulting multilayer M-II powder was acquired after filtration and at 45 °C vacuum drying for 24 hours. It's important to note that deionized water was used throughout the experiment to ensure purity of the final product.
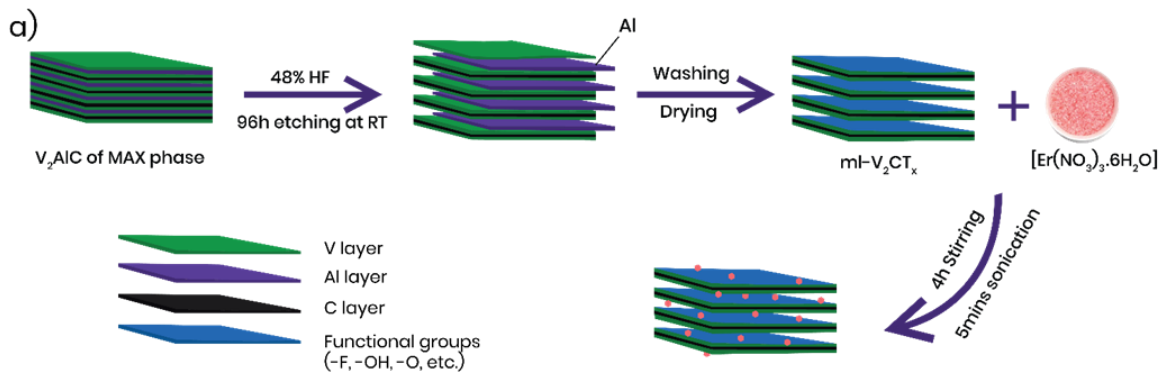
Figure 3.2: Synthesis of V_2CT_X and Er@V_2CT_X Nanocomposite

3.4. Synthesis of Er@Ti$_3$C$_2$Tx/V$_2$CTx Nanocomposites

Erbium nitrate Hexahydrate was added to V$_2$CTx/Ti$_3$C$_2$Tx MXene was denoted in terms of different atomic weights, with three ratios of Er@V$_2$CTx or Er/Ti$_3$C$_2$Tx nanocomposites (12.5%, 25%, and 50%) synthesized using a sonication method. The procedure involved dispersing 40 mg of V$_2$CTx in 40 mL of DI water and 12 mg of salt in 12 mL of DI water (1:1 volume ratio for each case). The solutions were stirred on a hotplate for 60 minutes, sonicated for 2 minutes, mixed, and magnetically stirred for an additional 2 hours, then sonicated for 2 minutes. The resulting solution was centrifuged at 4500 rpm and filtered using vacuum-assisted filtration and kept for drying overnight at 45˚C in a vacuum oven. The dried product was characterized further.

Table 3.3: Variables in the experiments that determine the composition of sample.

Material	V$_2$CTx MXene (ml)	(Er (NO$_3$)$_3$.6H$_2$0)	Atomic ratio (Er/V)
Er@V$_2$CTx	40	5	0.12:1
Er@V$_2$CTx	40	10	0.25:1
Er@V$_2$CTx	40	20	0.5:1

3.5. Fabrication of Electrode

For the fabrication of electrode, 0.8mg of active mass e.g. (Er@V$_2$CTx, V$_2$CTx, Er@Ti$_3$C$_2$Tx, Ti$_3$CTx) powders, acetylene black as a conductive agent, 35ml of Nafion (C$_7$HF$_{13}$O$_5$S.C$_2$F$_4$) binder and 0.1mg of Carbon Black was dissolved in 100µl of ethanol solvent in an 80:10:10 weight ratio. The mixture solution was kept for sonication for 10 minutes to create a homogeneous ink/slurry. The ink/slurry was then applied dropwise onto

a conductive Nickel foam (1.5 × 1 cm) and dried at 40°C in a vacuum oven overnight. The resulting electrode was then pressed at 500 psi for 10 seconds. Before casting the slurry on the Nickel foam, the foam was washed by sonicating it in DI water and ethanol for 10 minutes each and then dried on hot plate. This process ensured that the foam was clean and ready for slurry application.

3.6. Characterization techniques

To study the material properties different characterization techniques have been used which are explained below.

3.6.1. X-ray Diffraction

X-ray diffraction (XRD) analysis provides information of crystallinity and crystallite size of material.

Basic principle:

The basic principle of XRD is that the interaction of X-rays with the atoms of crystal, as a beam of X-rays is incident on a sample then X-rays scattered in different direction after interaction with atoms. The scattered X-rays interfere with each other and result in a characteristic pattern of diffraction.

X-ray production:

X-rays are produced when the electrons are targeted to the metal surface at some keV that knocked out the inner electrons in metal by energizing the electrons. When the electrons correspond to the upper shell fall into the vacancy in the lower shell then x-rays are emitted. The most commonly utilized metal targets are molybdenum and copper source. These emitted rays are called typical x-rays that have a definite wavelength which resembles the energy difference between two shells in the metal-based target.

XRD Mechanism:

In XRD mechanism involves the interaction of X-rays with atoms in material. When an X-ray beam falls on material then it scattered in different directions the crystal. The interference would occur between the scattered X-rays and resulting of interference produce the diffraction pattern which specific to each type of material crystal structure. This is due to the fact that the atoms in a crystal are arranged in a periodic lattice structure, and the interference between the scattered X-rays depends on the spacing between the atoms.
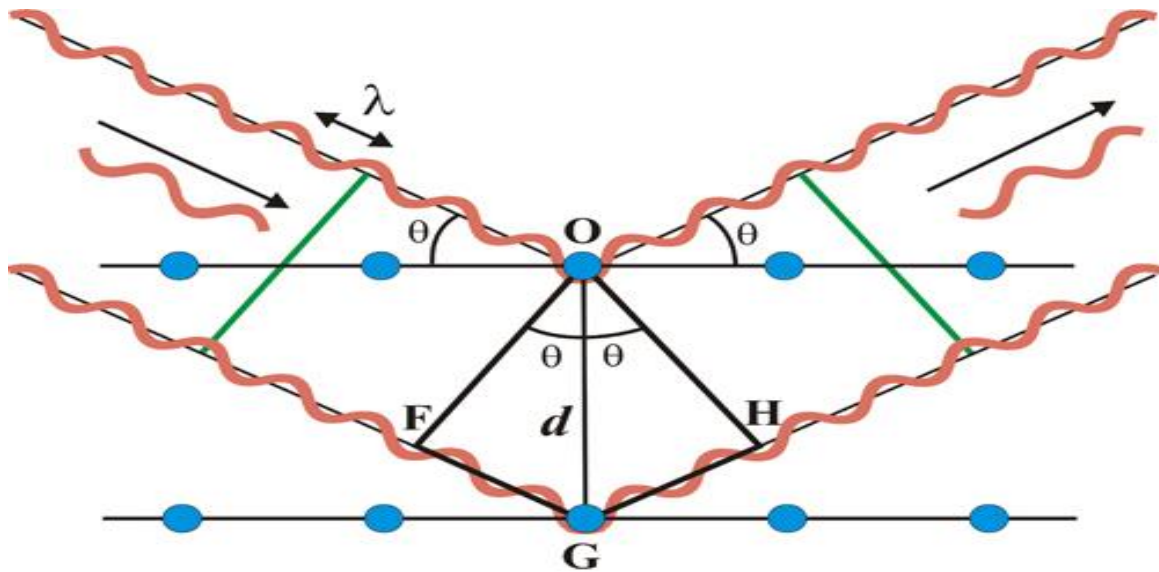
Figure 3.3: Bragg's law reflection

X-rays have wavelengths in range of 1Å to 100Å which comparable to inner atomic spacing (d_{hkl}) of the crystalline material. This causes the diffraction and scattering of the waves, collecting data about the material and its arrangement. From **figure 3.3**, Bragg's law tells that wavelength and angle of coming x-rays cause the constructive interference of dispersed waves:

$$n\ \lambda = 2d\sin\theta \qquad \text{…………………..(3.3)}$$

In equation, "n" is a positive integer, "λ" shows the X-rays wavelength, d shows interplanar spacing and θ represents the incident angle of waves. One of the parameters that XRD would measure the value full width at half of the maximum (FWHM) of peak that is utilized to measure the crystallinity of the material. A large value of the FWMH describes Bragg's peak that is wider and broader which shows the amorphous shape, and their crystallite size is also small. To find crystallite size use the Scherer equation used which is:

$$D = 0.54\lambda/\beta\cos\theta \qquad \text{……………………(3.4)}$$

D = crystallite size, β = FWHM value

XRD is a widely used technique in materials science, chemistry, and physics for analyzing the structure of crystalline materials, such as minerals, metals, ceramics, and polymers. It can provide information on the crystal structure, lattice parameters, and crystal planes orientations among other properties.

3.6.2. Scanning Electron Microscopy

Scanning electron microscopy (SEM) was utilized to study the surface morphology of prepared MXene nanocomposites. To get better resolution, materials were gold-sputtered before their SEM image and operating voltage of 3 kV had been utilized.

Basic Principle:

SEM technique is a mode of electron microscope which can produces high-resolution surface images of the sample. The basic principle of SEM involves the use of a beam of high-energy electrons which scanned over the surface of the material. In SEM, the electrons beam strike on the sample, and they produce signals then detected through detector and used them to generate an image.

Component of SEM

SEM components include:

Electron Source: In SEM, typically a heated tungsten filament or a field-emission source are being used as the electron source. The electron gun attaches with tungsten filament from which beams of electron emitted thermionically and have energies in range of 0.2 keV - 40 keV. The electron beam is focused on the two-condenser lens and then passes through the pair of scanning coils.

Electron Optics: The electron optics in an SEM are used to focus and direct the beam of electrons onto the sample. They include lenses, apertures, and other components. Typically, the final lens deflects the beam in the x-axis and y-axis which makes the raster scan over the rectangular area of material to analyze the surface morphology.

Sample Pan: It holds the sample and allows for its precise positioning and movement during imaging. The SEM makes a raster scan of the sample and position of the electron beam combined with the intensity of the perceived signal.

Detector: The detector in an SEM is used to collect signals which are produced by the interaction of the electron beam with material and amplify. The most common type of detector used in SEM is the secondary electron detector.

Imaging System: The imaging system in an SEM is used to convert the signals collected by the detector into an image. This typically involves the use of a cathode ray tube or other display device.
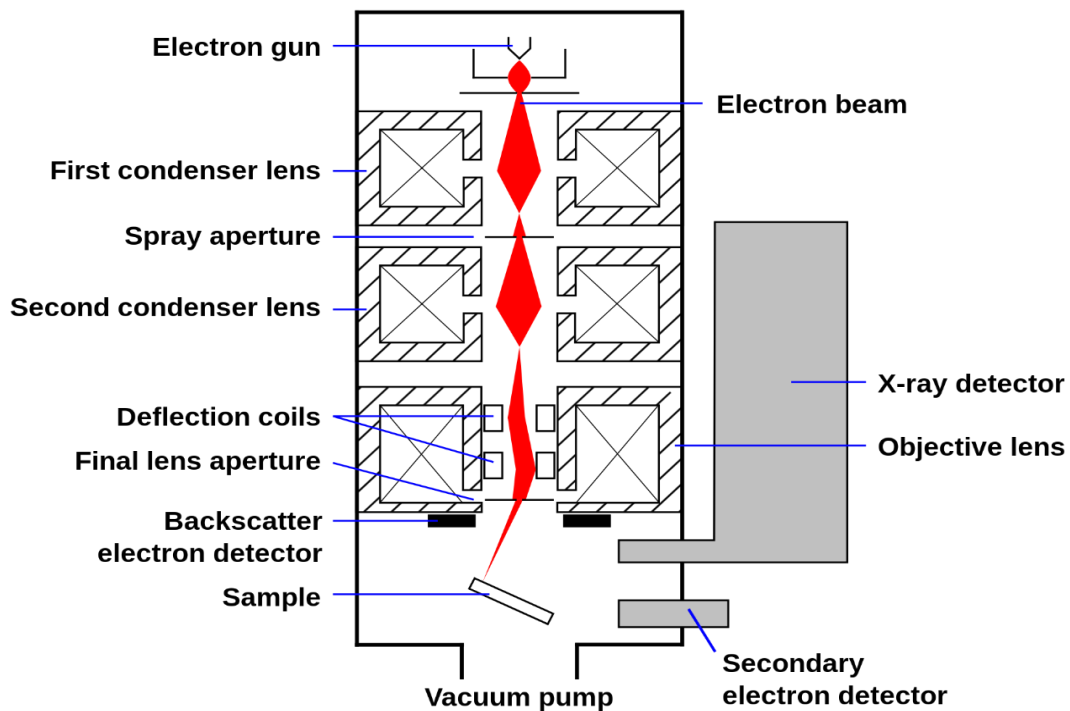
Figure 3.4: Schematic representation of SEM working mechanism.

3.6.3. Energy-Dispersive X-mechanism spectroscopy

Energy-Dispersive X-ray (EDX) s technique has been used to analyze chemical composition of a sample by detecting the X-rays generated from the sample when it is bombarded with high-energy electrons.

Basic principle and Working:

In EDX analysis high energy electrons interact with the atoms of the material. This interaction causes the ejection of electrons from the innermost atomic shells. As a result, the atoms become ionized and move to a higher energy state. When the atoms return to their original energy state, they emit X-rays that are characteristic of the elements present in the sample. These X-rays are detected by an X-ray detector, which is capable of distinguishing the different energies of the X-rays emitted by different elements. The energy of emitted X-rays is proportional to the energy difference between the two energy states of the atoms, which is specific to each element. Thus, by measuring the energies of the emitted X-rays, the elements present in the sample can be identified and their relative abundance can be determined.

3.6.4. Fourier Transform Infrared Spectroscopy

Fourier transform infrared (FTIR) spectroscopy is mostly used to identify and distinguish the molecules present in material. This technique provides information about the chemical bond stretching in material and it is also a non-destructive technique.

In FTIR analysis commonly we observed data in 3 parts. First the peak position, secondly peak width and peak intensity. The peak position is exclusive for every material so we can recognize the material. The peak width describes the type of functional group attach and peak intensity measures the vibration energy of the molecule.

Basic principle:

The basic principle of FTIR spectroscopy, the use of an infrared beam that is passed through a sample. As the beam interacts with the sample, some of the radiation is absorbed by the sample molecules and some is transmitted through the sample. The transmitted radiation is then detected and analyzed using a detector. The resulting spectrum, which represents the absorption of radiation at different frequencies, is used to identify the molecular structure and composition of the sample. The different molecules in materials are present with a different structure which shows the different spectrum.

Working:

Infrared Source: The infrared source is used to generate a beam of infrared radiation that is directed towards the sample.

Sample Compartment: The sample compartment is the area where the sample is placed for analysis. Typically, it is a sealed chamber that is designed to prevent interference from external sources.

Interferometer: The interferometer is used to split the beam of infrared radiation into two paths, which are then recombined to produce an interferogram. The interferogram contains information about the sample's absorption spectrum.
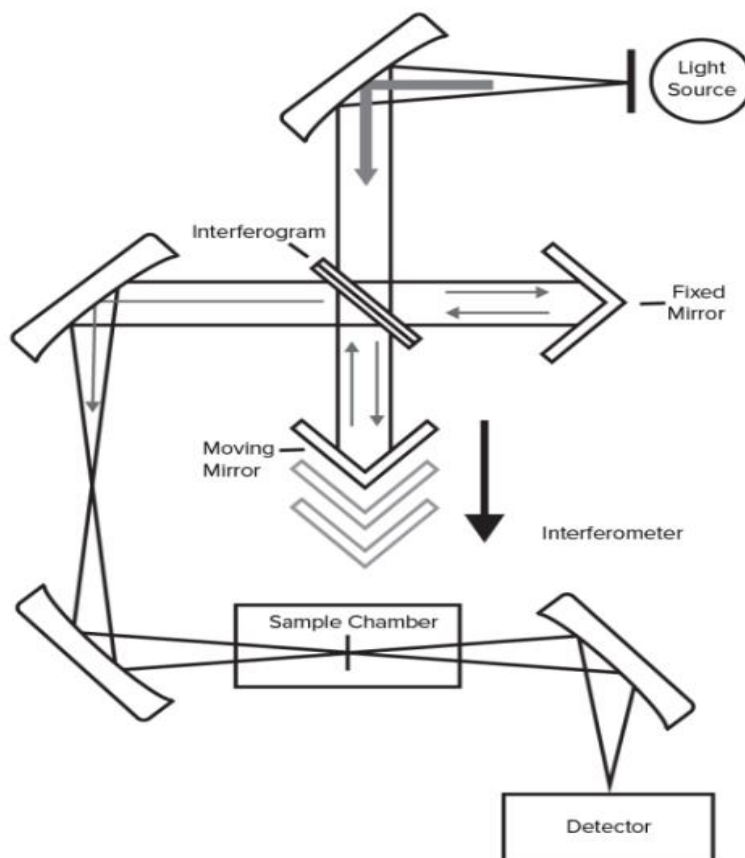
Figure 3.5: Representation of FTIR spectrometer parts

Detector: The detector is used to measure the interferogram and convert it into a spectrum, which represents the sample's absorption of radiation at different frequencies.

Data Analysis Software: The data analysis software is used to process the raw data and generate a spectrum, which can then be analyzed to identify and quantify the composition of sample.

3.6.5. Raman Spectroscopy

Basic principle:

The technique is based on the inelastic scattering of light which happens when photon interacts with a molecule and cause it to vibrate. It provides chemical and structural information through characteristics Raman "fingerprint" and gave the information by detecting the signal through sample scattering by studying the vibrational modes using Raman Spectroscopy.

Explanation:

When a sample is illuminated with a laser beam, some of the photons are scattered elastically, meaning that they maintain their original energy and frequency known as Rayleigh scattering and could not provide useful information, while others are scattered inelastically, losing or gaining energy and producing a shifted frequency. The shifted frequency is called the Raman shift or scattering, and it is characteristic of the vibrational modes of the molecules in the sample.
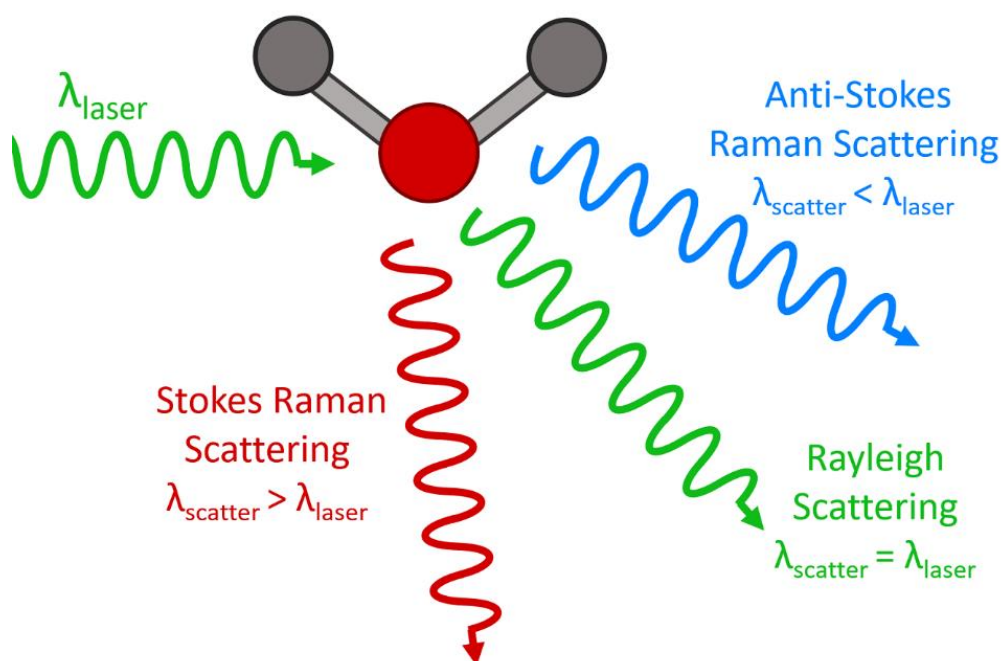
Figure 3.6: Interaction of laser light with samples and types of scattering

By the study the vibrational modes of materials using Raman analysis in term of scattered light intensity as function of frequency which help to identify and investigate to understand the types of chemical bonds as well as their relative strengths and orientations in the analyzed materials. This information can be used to determine the composition, structure, and even the orientation of the molecules in the sample.

Raman spectroscopy gives the distinct fingerprint spectrum of chemical for a particular material (molecules) which could quickly identify the material. In addition, Raman spectrum provides information related to structure, identity, impurity and phase of material.

3.6.6. Electrochemical Characterization

Electrochemical experiments are typically employed to investigate the behavior of electrodes immersed in an electrolyte when subjected to externally applied potential or triggered currents. In this research project, the efficiency of electrocatalysts was evaluated using two primary techniques: cyclic voltammetry and linear sweep voltammetry. Chronoamperometric measurements were used to examine the stability of the catalysts, while electrochemical impedance spectroscopy was utilized to investigate the diffusion resistance and charge transfer resistance of the prepared samples. This method permits a thorough evaluation of the electrochemical properties and efficacy of the investigated electrocatalysts.

3.6.6.1. Potentiostat

A potentiostat is an electronic device used in electrochemistry to control the potential difference (voltage) between an electrode and a reference electrode while measuring the flow of current through the electrochemical cell. It enables precise control of the electrode potential, which is crucial for the study of various electrochemical processes, therefore an essential tool in electrochemical research and analysis. The energy storage characteristics were examined using a three-electrode electrochemical workstation (GAMRY B1010).

Figure 3.7: Representation of Potentiostat apparatus.

A typical potentiostat consist of three electrode including working electrode (anode), reference electrode (Platinum wire) and counter electrode (conventional silver/silver chloride (Ag/AgCl). The electrochemical reaction take place on working electrode. While, the reference electrode in potentiostat provides a stable reference potential against which potential of working electrode needs to be controlled. The circuit completion and flow of circuit in system process through the counter electrode.

In potentiostat function, first control potential difference generated between working electrode and reference electrode. Then measuring the current that is subsequently flowing through the electrochemical cell as a result of this controlled potential. Potentiostat are used to precisely control electrochemical reactions by adjusting the potential so that there is a constant potential difference generated between the working and reference electrode respectively. This allows the reaction to be precisely controlled.
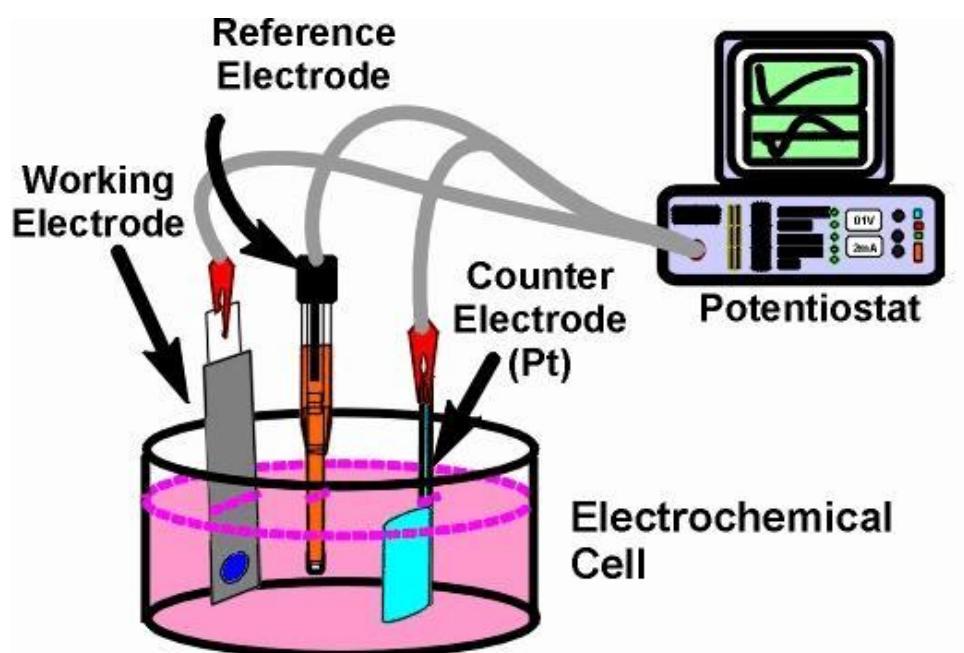

Figure 3.8: Representation of three-electrode setup of potentiostat apparatus.

3.6.6.2. *Linear sweep voltammetry*

Linear sweep voltammetry (LSV) is known as electrochemical system which can examine behavior of an electrochemical system by applying a linearly increasing potential to the working electrode and determining the resulting current. In LSV working principle consist

of sweeping the potential difference through working electrode at a constant rate over a defined voltage range, typically from a starting potential to an ending potential, while recording the current response[60]. The plot of current versus potential is called a voltammogram. It tells us about the system's redox behavior, electrochemical kinetics, and other electrochemical properties.

The parameters of a recorded linear sweep voltammogram are influenced by several factors, including:

- electron transfer reaction(s) rate
- electroactive species
- scan rate voltage

Changes in the scan rate can result in different current responses, as shown in Figure 31, where various voltammograms acquired at different scan rates exhibit similar shapes but different total currents. This can be attributed to the length of the scan recording and the thickness of the diffusion layer. A slower scan rate results in a longer time to capture the voltammogram, leading to a larger diffusion layer above the surface of electrode. This larger diffusion layer leads to a lower flux of electroactive species towards the electrode surface, resulting in lower currents. Conversely, at higher scan rates, the diffusion layer is thinner, and the flux towards the electrode surface is higher, resulting in higher currents. Therefore, the scan rate has a significant impact on the voltammogram parameters, and careful consideration of scan rate effects is important for accurate interpretation of the results.
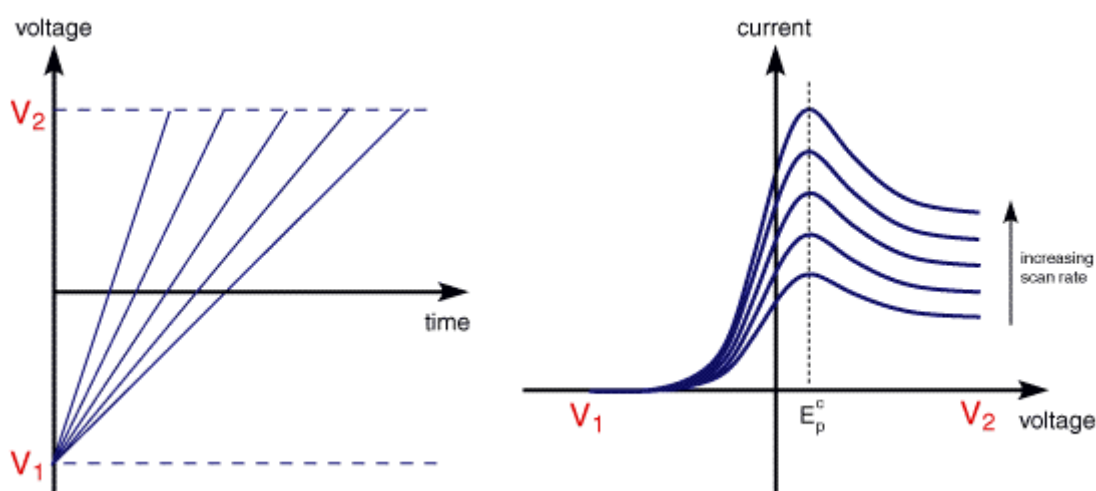
Figure 3.9: Measuring the LSV at different scan rates.

3.6.6.3. Electrochemical Impedance spectroscopy

The technique Electrochemical Impedance Spectroscopy (EIS) is used in electrochemistry to analyze the electrical behavior of electrochemical systems. It involves applying a small amplitude sinusoidal voltage or current perturbation to a system and measuring the resulting response in terms of impedance. The basic principle of EIS is based on the fact that the impedance of an electrochemical system changes with frequency due to the different rates of charge transfer and mass transport processes at different frequencies[61]. At low frequencies, the impedance is dominated by processes such as charge transfer and diffusion, while at high frequencies, it is influenced by processes such as capacitance and inductance. Electrochemical impedance spectroscopy (EIS) employs low amplitude alternating current (AC) voltages at different frequencies to characterize the transient behavior of chemical processes. This technique involves applying a known potential difference between working electrode counter electrode through an electrolyte, utilizing an electrode framework that consist of working, reference and counter electrode system.
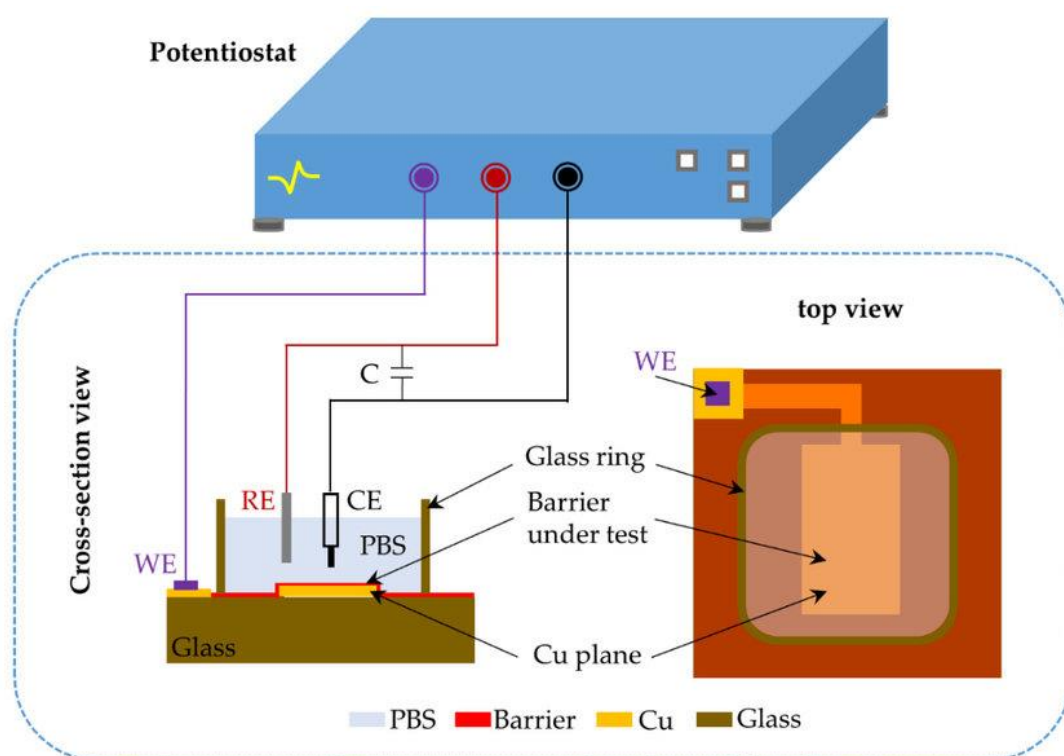
Figure 3.10: Representation of electrochemical impedance spectroscopy (EIS) test setup.

3.6.6.4. Chronoamperometry

The technique Chronoamperometry is based on electrochemical system and used to analyze the behavior of an electrochemical system under a constant applied potential. In

chronoamperometry, a fixed potential difference applied to working electrode and electrochemical cell. The result of applying potential difference cause the current flow through the system and it is determined as a function of time.

In chronoamperometry, it's working mechanism based on Faraday's law of electrolysis. It states that the oxidation or reduction of material at an electrode must be proportional to quantity of charge moving through electrode. In this process a constant potential difference is applied to the working electrode system through potentiostat system and cause to produce the current and it measured as a function of time. This provides the information about electrochemical processes occurring at the surface of electrode including the electron transfer rate, concentration of electroactive species and kinetics of the electrochemical reaction. By analyzing the time-dependent current behavior, valuable insights into the underlying electrochemical mechanisms and kinetics can be obtained, making chronoamperometry a powerful tool in electrochemical research and analysis[62].

Chapter 04: Results and Discussion

4. Materials Characterizations

In the following section, we will present the outcomes of our investigation on the synthesized materials, namely V_2CTx, Ti_3C_2Tx MXene and $Er@V_2CTx$, $Er@Ti_3C_2Tx$ nanocomposites at varying concentrations, utilizing a range of characterization techniques. These techniques are utilized to study the morphology, structural characteristics, and elemental compositions of the materials. Additionally, the materials' performance in energy storage applications will be evaluated.

Several characterization techniques will be discussed in this study, including:

- X-ray diffraction spectroscopy (XRD)
- Scanning electron microscopy (SEM)
- Energy dispersive spectroscopy (EDX)
- Fourier transform infrared spectroscopy (FTIR)
- Raman spectrometry

The material's phase identification and structural investigation are conducted using XRD with a (Bruker D8 Advance instrument, Germany). Morphology and elemental concentration are determined through SEM and (EDS. Furthermore, FTIR and Raman spectroscopy are performed to gain insights into the nanocomposite samples of $Er@V_2CTx$ and $Er@Ti_3C_2Tx$.

Nanocomposites were formed by combining $Er\,(NO_3)_3.6H_2O$ salt with V_2CTx in various ratios, namely 0.5:1, 0.25:1, and 0.15:1, marked as S3, S2, and S1. Based on the results, the nanocomposite among these ratios of 0.15:1 displayed the most promising performance for water-splitting applications in a 1M KOH electrolyte.

4.1. X-Ray Diffraction of V_2CTx MXene

Standard reference X-ray powder diffraction (XRD) patterns using JCPDS No. (29-0101) were utilized to identify the phase of as-received V_2AlC MAX-phase in figure 4.1. The presence of two distinct peaks at 13.4º and 41.2º, corresponding to (002) and (103) planes, respectively, in the XRD pattern validates the MAX phase structure. The sharpness of these peaks indicates high crystallinity and purity of the precursor material. For the synthesis of V2C MXene, a chemical etching route was employed, and the XRD pattern of MAX phase

and HF-treated MXene in figure 4.1 confirms the success of the etching process. The decrease in intensity and shift in peak positions, to 9⁰ with a c-lattice constant 19.94 Å and 39.8⁰ with c-lattice constant 19.94 Å, of the (002) and (103) peaks respectively corroborate this claim. Furthermore, the shift of (002) peak towards lower angle suggests an increased the interlayer spacing, indicating successful exfoliation of the MXene layers through the removal of the Al layer from the MAX phase. However, despite this, some residual peaks related to V2AlC MAX phase are still noticeable, signaling the presence of unetched MAX phase in MXene sample.

Crystalline size (d) of the peak is find by the Debye-Scherer equation[63]:

$$d = \frac{k\,\lambda}{\beta\,\cos\theta}$$

Where,

λ = wavelength $\qquad\qquad\qquad\qquad$ θ = diffraction angle

K = Scherrer constant and equals 0.89 $\qquad$ β = full width at half-maximum

4.1. X-Ray Diffraction of Er@V$_2$CTx MXene Nanocomposite

X-ray diffraction (XRD) was used for analysis of crystallographic data regarding the prepared materials. XRD results of pristine V$_2$CTx and Er@V$_2$CTx nanocomposites with increasing proportions which has been depicted in Figure 4.1. Eliminating of an aluminum layer from the MAX sheets and the presence of intercalated water molecules which resulted in increase of c-lattice parameter. Upon addition of Er onto V$_2$CTx, the (002) peak shifts to around 5.90^0, accompanied by a corresponding increase in the c-lattice parameter to 29.9 Å in the case of S1 (0.12:1) nanocomposite. The diffraction peak (002) broadens and shifts to lower angles by decreasing doping ratio which indicating the attachment of Er to the V$_2$CTx layers. Given that the size of a single Er atom (Ionic size) is 1.75 Å (+3) it is estimated to intercalate into the 2D layers of MXene and attach to MXene surface as a termination group. This implies that Er atoms are incorporated into the nanocomposite structure, causing changes in the XRD pattern.
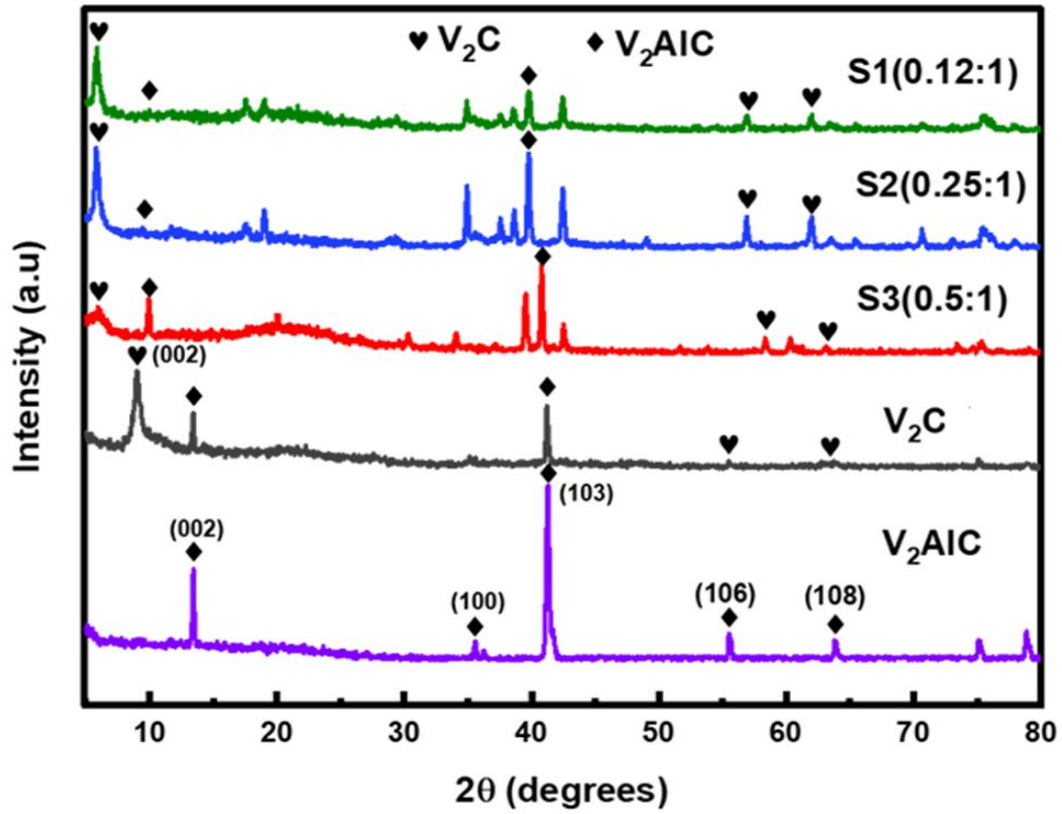
Figure 4.1: XRD Analysis of V_2CTx MXene and Nanocomposite

Table 4.1: Shows corresponding peak shift and c lattice parameter.

Samples	Bragg's Angles	d-spacing (Å)	Lattice Constant (Å)
	2θ	$\dfrac{\lambda}{2\,Sin\,\theta}$	$d_{hkl} * \sqrt{(h^2 + k^2 + l^2)}$
MAX	13.45	6.5	13.1
MXene	8.95	9.87	19.7
S1	5.8	15.22	30.4
S2	5.85	15	30.1
S3	5.95	14.8	29.6

4.2. SEM Analysis

MXene and its nanocomposite structure with Er were analyzed by utilizing scanning electron microscopy (SEM) with an energy-dispersive spectrometer (EDS), with a range of 10 kV-20 kV. The aim was to investigate the microstructure and surface morphology of prepared Mxene and Mxene based nanocomposite materials. Previous research on V_2AlC reported characteristic compact ceramic particles. Micrographs of the MAX following HF treatment were presented in Figure 4.2 (a,b,c). The SEM analysis revealed that the 2D V_2CTx was formed by selectively removing most of the Al atoms from the V_2AlC precursor, using a 49 percent hydrofluoric acid solution[64].

Immersing V_2AlC MAX particles in HF etching solution exhibited characteristic layered morphology in SEM pictures of V_2CTx. SEM investigations revealed no MAX particles. In addition, scanning electron microscopy (SEM) shows that V_2CTx unique accordion-like stacking MXenes were created, which is confirmation that MXene was synthesized[65].

The intercalation/decoration of Er on surface of MXene layers was found to resulted in roughness of surface. The presence of Er on the surface of V_2CTx MXene was clearly visible, suggesting successful intercalation.
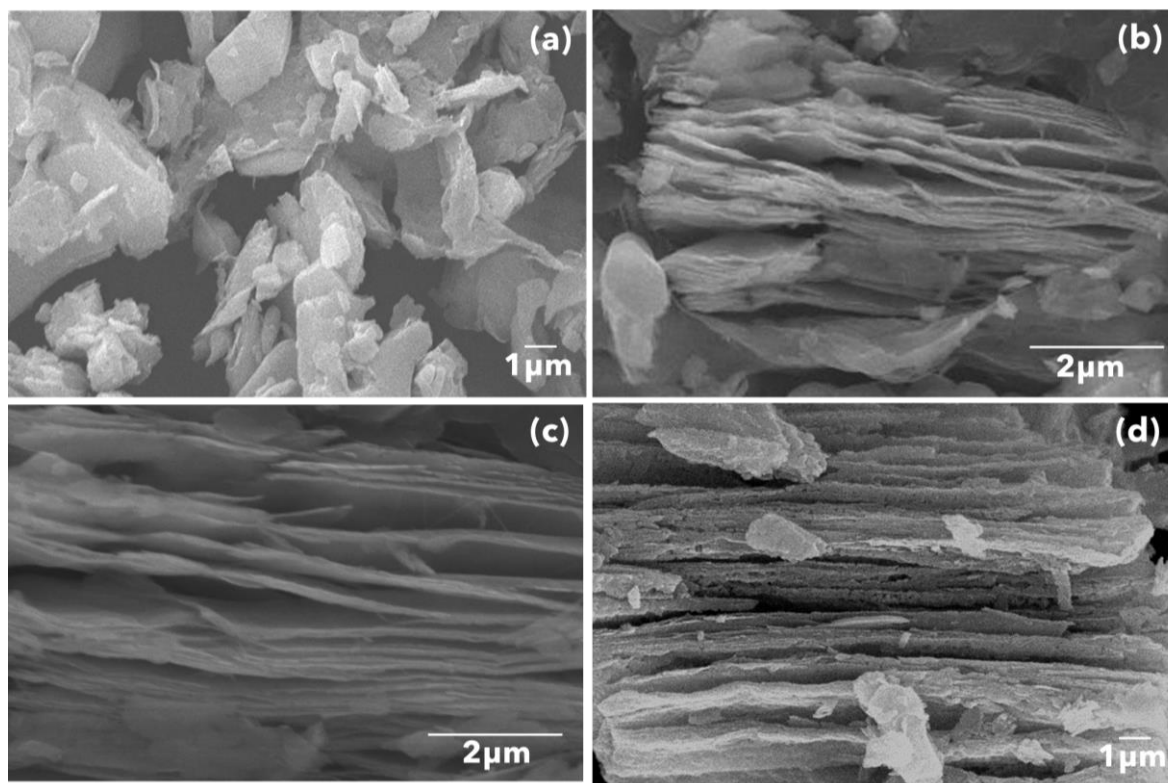
Figure 4.2: Representation of SEM analysis of V_2CTx MXene and Nanocomposite.

4.3.   EDS analysis

The elemental mapping of the nanocomposite (S1) hybrid was accomplished through the use of EDX. In the course of the chemical etching procedure, the findings indicate that a negligible amount of aluminum atoms originated from MAX that had not yet etched. The EDX analysis also uncovered the presence of the elements oxygen (O) and fluorine (F) in the multilayer structure are present in multilayer V_2CTx MXene, and that they are coupled to the surface as functional groups that were attached during the process of synthesis. To this day, no MXene has been successfully synthesized without having surface terminations. The presence of Er is validated by the nanocomposite EDX spectrum.

Figure 4.3: Represents the EDX analysis of V_2CTx MXene and Nanocomposite.

4.4.   FTIR analysis of V_2CTx MXene

The FTIR spectrum of V_2CTx MXene powder typically shows several characteristic peaks, which can provide insights into the structural and chemical properties of the material. Here

is a detailed discussion of some common features that may be observed in the FTIR spectrum of V_2CTx MXene powder:
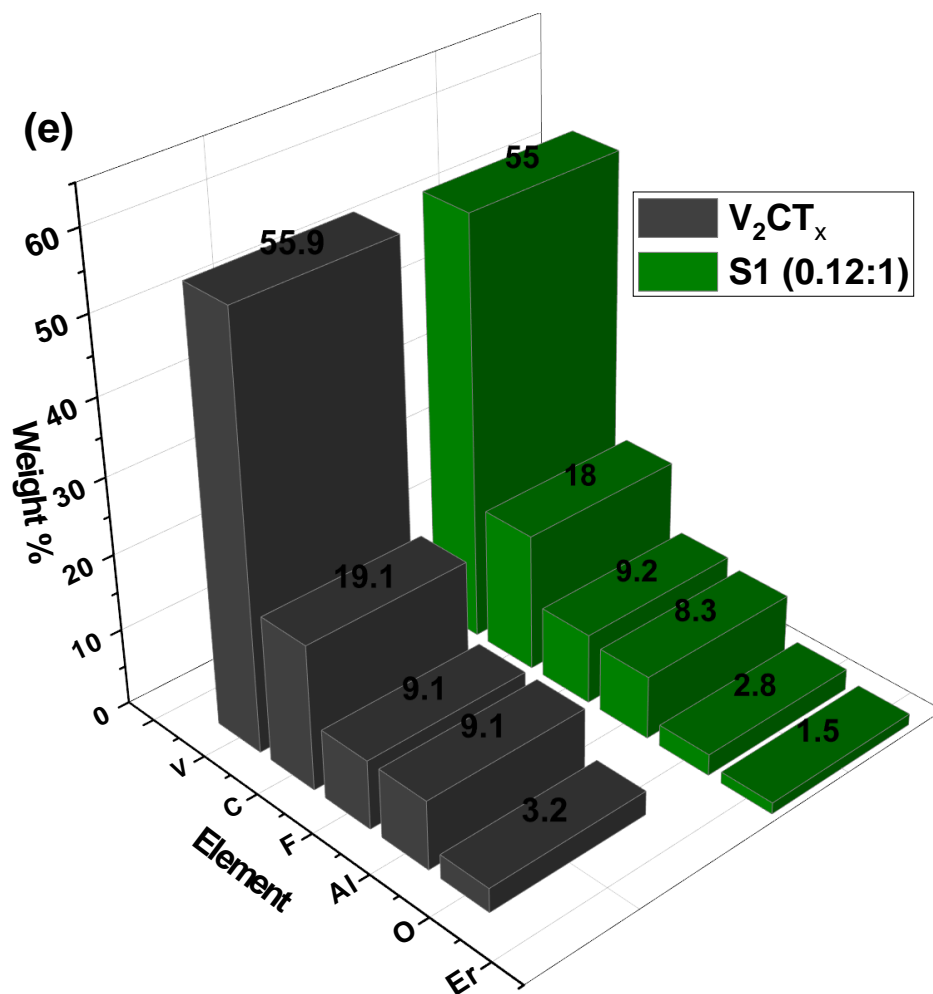
The FTIR spectra of V_2CTx MXene (Fig. 4.4) reveal characteristic absorption bands in the range of 400 - 4000 cm^{-1}. The observed absorption bands are located at 505 cm^{-1}, 596 cm^{-1}, 1148 cm^{-1}, 1632 cm^{-1}, 1086 cm^{-1}, 3428 cm^{-1}, and 2922 cm^{-1}. The fingerprint region of the FTIR spectra of V_2CTx MXene exhibits bands at 505 cm^{-1}, 1148 cm^{-1}, and 1632 cm^{-1}, which can be attributed to the stretching vibrations of V-C, C-O, and C=O bonds, respectively[66]. The peak centered at 3428 cm^{-1} is attributed to the stretching modes of the hydroxyl group (-O.H.) which indicate the intercalation of water molecules into the vanadium oxide layers after the H.F. treatment. The absorption peak at 1086 cm^{-1} attribute the C-F vibration and the peak detected at 596 cm^{-1} attributes the V-O bending vibration[67]. The band detected at 2922 cm^{-1} is ascribed to C-H bond stretching vibration.
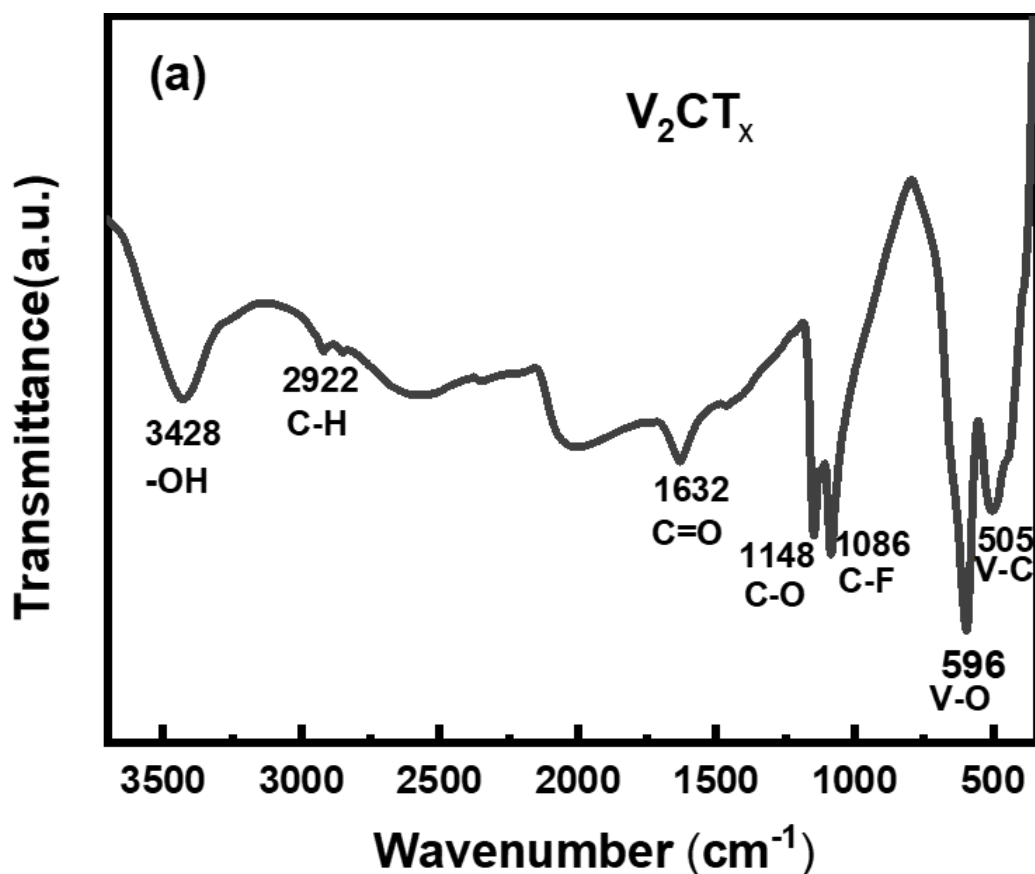

Figure 4.4: Represents the FTIR Spectra of **a)** V_2CT_X

4.5. FTIR spectra of Er@V$_2$CTx Composite

In the infrared spectra (IR) of V$_2$CTx MXene and Er@V$_2$CTx composite (1.12:1) referred as S1, the fingerprint regions and main functional groups have been successfully identified. The FTIR spectra of the composite show clearly visible bands corresponding to V$_2$CTx and S1 composite in figure 4.5. The spectral range of 500-1500 cm^{-1} is commonly referred to as the fingerprint region in FTIR spectroscopy. The spectral range above 1500 cm^{-1} in a given spectrum indicates the presence of functional groups. Notable peaks at 3425 cm^{-1}, 2919 cm^{-1}, 2500 cm^{-1}, and 1632 cm^{-1} are observed within this region, which are characteristic of certain functional groups. The presence of sharp and well define peaks in the FTIR spectra indicates the successful formation of a nanocomposite, as it suggests the occurrence of specific stretching vibrations associated with the composite material. The FTIR spectrum of Er@V$_2$CTx revealed peaks at 3425 cm^{-1} and 1632 cm^{-1}, which are indicative of the presence of -OH and C=O functional groups, respectively. However, in the spectrum of S1 nanocomposite, these peaks were no longer observed, indicating the absence of C-O and C-F bonds in the nanocomposite.
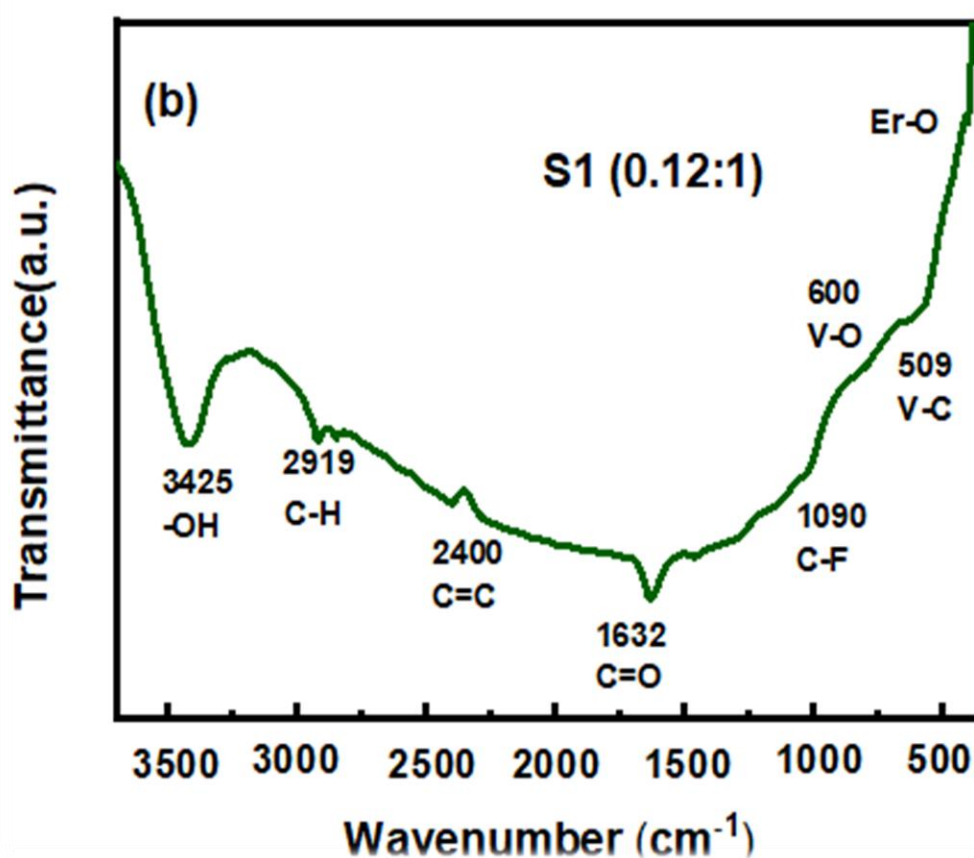

Figure 4.5: FTIR Spectra of **b)** S1 nanocomposite

4.6.   Raman Spectroscopy

The Raman spectra of V$_2$CTx MXene after etching at room temperature for 96 hours has been are displayed in Figure 4.6a. The spectra demonstrate a high-frequency peak at 282 cm^{-1} which can be attributed to enhanced interlayer spacing. Additionally, four peaks at 406 cm^{-1}, 505 cm^{-1}, 682 cm^{-1}, and 989 cm^{-1} are observed, corresponding to the active vibration modes of terminated V$_2$CTx MXene. These peaks are indicate termination of surface such as -O, -F, and -O.H., on the MXene. Thus, the Raman data confirms the successful synthesis of V$_2$CTx MXene. However, it is important to identify the numerous In-plan Eg bands have been reported for V$_2$CTx MXene due to variations in etching parameters. The peak at (230-470) cm^{-1} is consistent with the Eg model of V$_2$CTx, while the peak at 682 cm^{-1} was assigned to the A1g model of V$_2$C(OH)$_2$. Furthermore, the peak at 505 cm^{-1} is related to active carbon mode A1g correspond to V$_2$CF$_2$ and V$_2$C(OH)$_2$. The Eg model is associated with the in-plane vibration of V atoms, whereas the A1g model is linked to the out-of-plane vibration of V atoms. These observations suggest that the Raman spectra of V$_2$CTx MXene exhibit different peaks corresponding to specific vibrational modes and models, depending on the etching parameters used during synthesis fig4.6b.

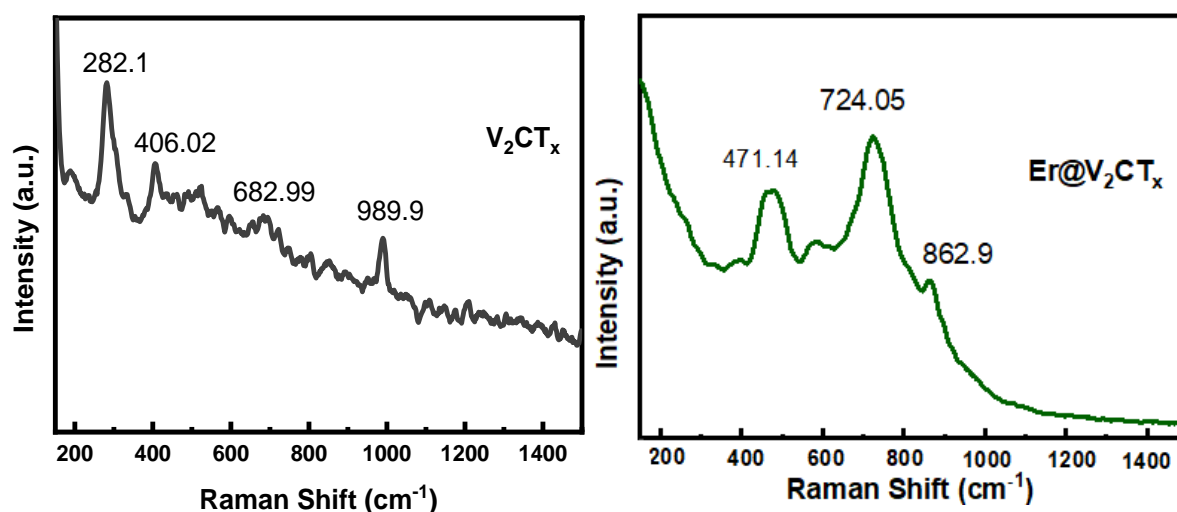**Figure 4.6:** representation of Raman Spectra of V$_2$CTx MXene and Nanocomposite.

4.7.   Electrochemical Analysis and measurements

On a Gamry Interface 1010B potentiostat with a three-electrode system[68] in a 1M KOH electrolyte, electrochemical testing was conducted. A functional electrode was used to evaluate as-synthesized MXene and its composites with variable ratios. Ni foam served as

the current collector for the active electrode, while a Platinum wire and an Ag/AgCl (3.5M KCl) electrode served as reference and counter electrodes respectively.

4.7.1. Linear Sweep Voltammetry (LSV)

V2CTx MXene and Er@V_2CTx LSV findings are compared here. The polarization curves' Tafel slope and overpotential indicate activity. Changes in the overpotential or current as a function of time are used to characterize stability.

4.7.2. Oxygen Evolution Reaction (OER)

For determining overpotential to standard 10 mA cm^{-2} (Π@10 mAcm^{-2}) [69], a standard diagram of current density versus voltage is utilized. This involves measuring the generated current in relation to the provided voltage using a potentiostat. The resultant current density is then determined by dividing current by catalyst's surface area on the electrode. Typically, the oxygen evolution reaction commences at the end of the non-faradaic zone, at which point the onset potential is identified. A lowered onset potential indicates that an OER catalyst is better.

Using LSV polarization curves, Figure 4.7a depicts the response of the electrochemical system to V versus RHE stimuli. Er-decorated V_2CTx sheets have a lower overpotential required to attain 10 mA cm^{-2} compared to pristine V_2CTx. Overpotentials of S1, S2, S3, and Pristine V_2CTx were 370, 400, 430, and 480 mV respectively with a bulk concentration of 1 mg cm^{-2}.

Er salt loaded homogeneously on 2D sheets act as a conductive agent with a wide surface area, facilitating ion transport via the assurance of short conductive paths at the interface. Additionally, a small quantity of Ag intercalation into the multilayer structure exposes additional MXene sheets. As the amount of Er@V_2CTx in the system evolves, the rate of reaction slows down. The increased concentration, as observed in the SEM micrographs, covers the 2D sheet structure, which may lead to blockages and a reduction in activity. The Tafel slope of each material that was studied during this investigation is depicted in Figure 4.7b.

To evaluate the kinetics and stability of the OER, the respective catalysts' overpotentials were computed (figure 4.7c). In comparison to the pure V2CTx MXene (143 mV/dec) and the computed tafel slope of S1 composite (354 mv/dec) was the lower as compared to other composite's materials. For S1, S2, S3 and pristine MXene, the Tafel slopes were (131, 175,

201 and 354 mV/dec, respectively). Er actively supports OER, since pure V_2CTx nanosheets are relatively show smaller activity. To improve OER kinetics, V_2CTx nanosheets can be used to facilitate the transfer of electrons from Er to the V_2CTx matrix.

Figure 4.7: a) OER Polarization Curves **b)** Overpotential at 10mAcm^{-2} and 20mAcm^{-2} for S1, S2,S3 and V2CT$_X$ **c)** Tafel slope for S1,S2,S3 and V_2CT_X

4.8. Hydrogen Evolution Reaction Performance

Linear sweep voltammetry (LSV) technique was implemented on prepared Mxene based materials with 10 mVs^{-1} scan rate and HER performance of synthesized samples in a 1M KOH solution was evaluated[69]. The results indicated that the S1 (0.15:1) demonstrated significantly better HER performance than either of its components V_2CTx MXene or Er (figure 4.8 a). This indicates that the design of the Er@V_2CTx supports the catalytic process by stimulating the charge movement from catalyst to electrode.

As-prepared samples for HER performance have been evaluated under same circumstances. The polarization curves for all materials have been shown in figure 4.8 b. In comparison to the pure V2CTx MXene (209 mV/dec) and the computed Tafel slope of S1 composite (107 mv/dec) was the lower as compared to other composite's materials in figure 4.8c.
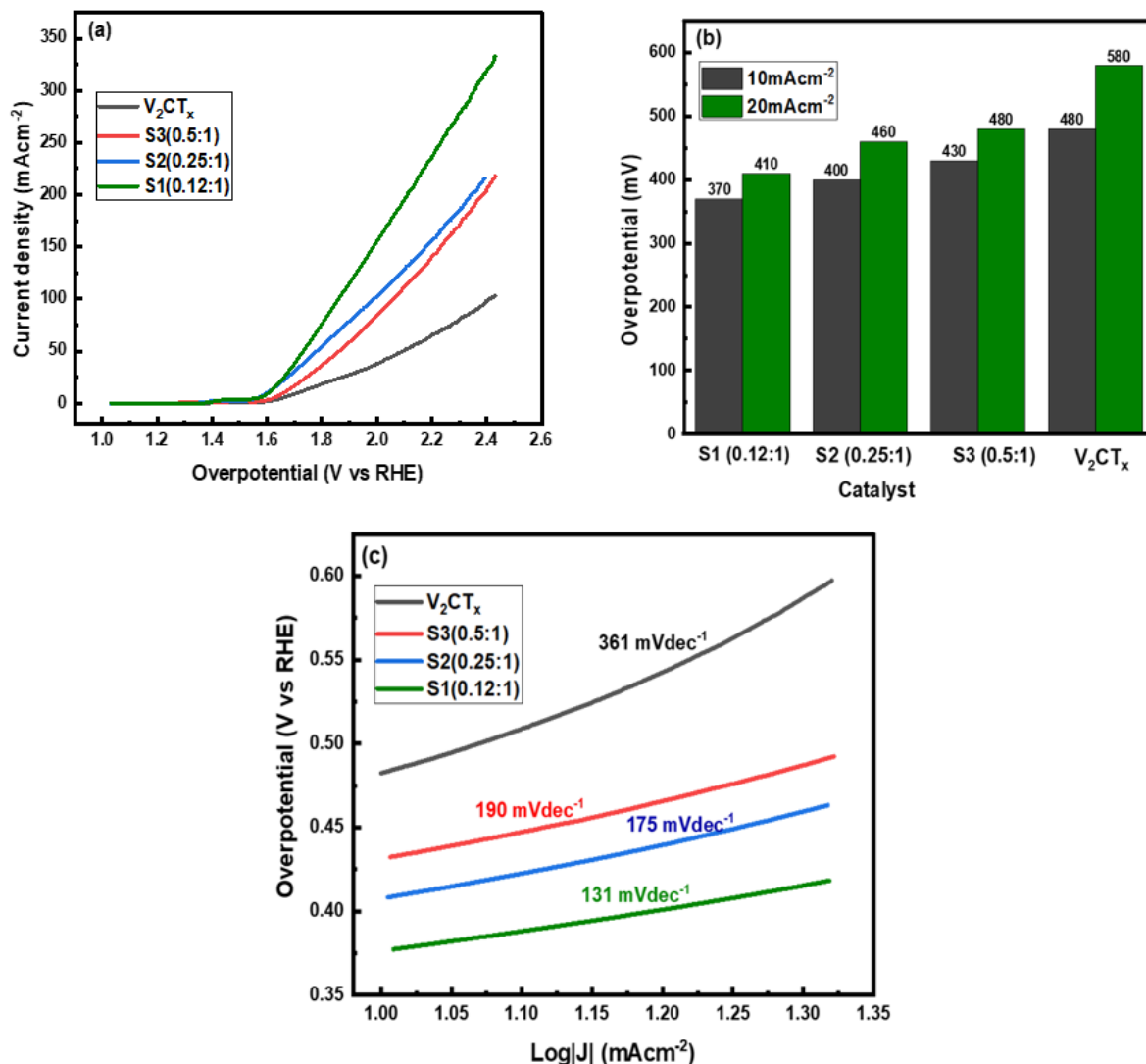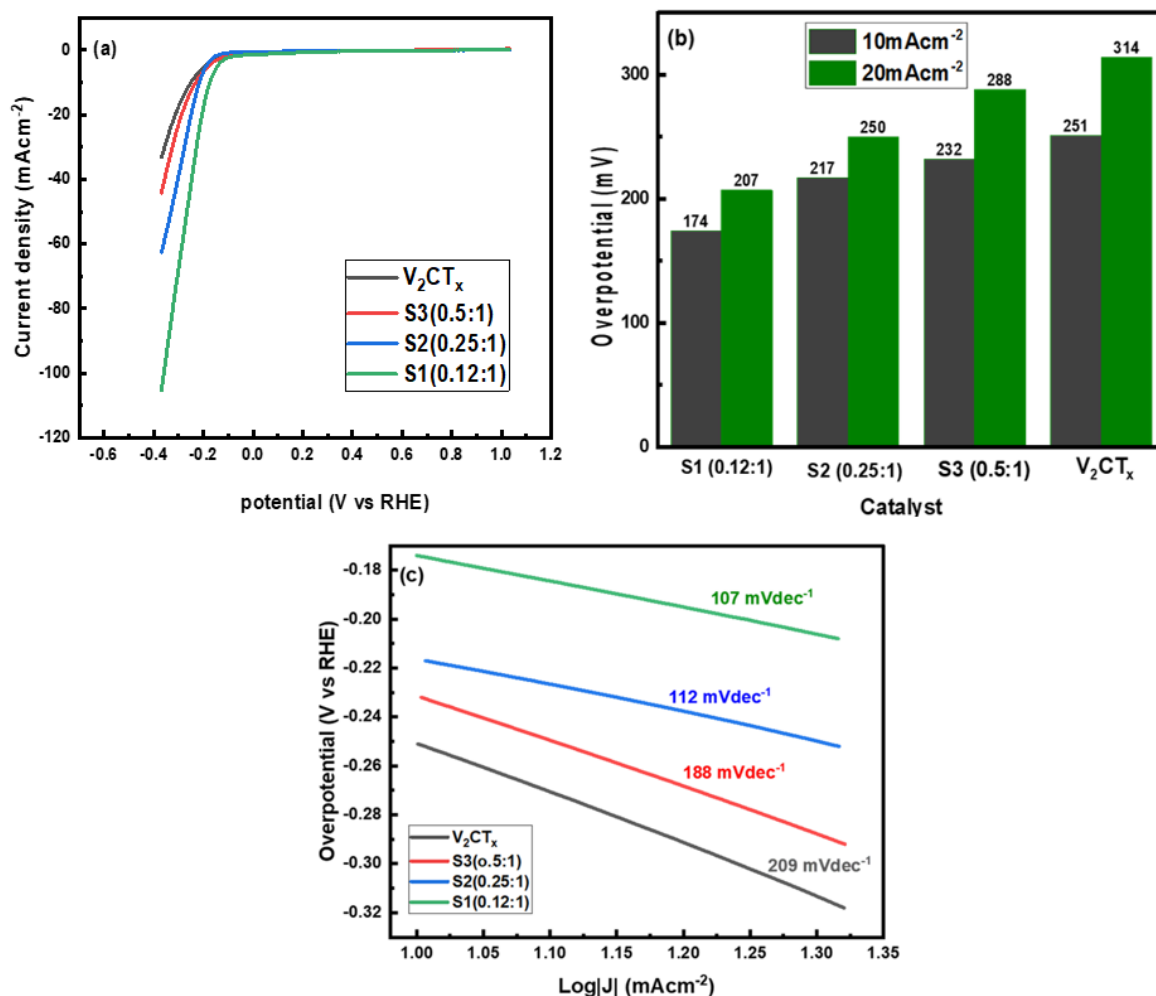

Figure 4.8: a) HER Polarization Curves **b)** Overpotential at 10mAcm^{-2} and 20mAcm^{-2} for S1, S2,S3 and V$_2$CT$_X$ **c)** Tafel slope for S1,S2,S3 and V$_2$CT$_X$

4.9.   Chronoamperometry

Durability and stability are crucial factors in evaluating the efficiency of an electrocatalyst. To assess these properties, chronoamperometry was conducted at a potential of 0.6V and 10 mVs^{-1} scan rate over a duration of 14 hours, as illustrated in Figure 4.9. The results demonstrate that the bare MXene exhibited instability, with a significant drop in current density by 48% within the initial few hours. However, upon the addition of Samarium, the

composite demonstrated enhanced stability throughout the test, maintaining a current density of 80% of the maximum value.
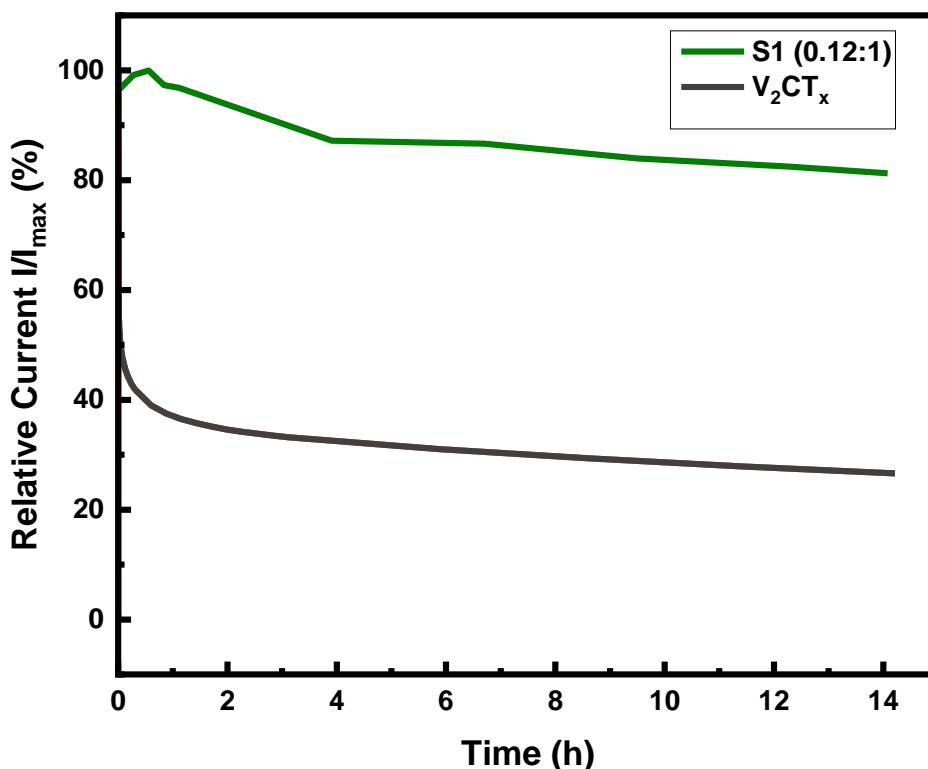
Figure 4.9: Chronoamperometry Stability measurements of S1(0.12:2) and V2CTx MXene

4.9.1. Electro Impedance Spectroscopy

The technique Electrochemical impedance spectroscopy (EIS) was utilized to analyze the synthesized V_2CTx and S1(0.12:1) nanocomposite electrocatalysts kinetics. EIS measurements have been performed between 0.1 Hz - 20 kHz frequency range and utilizing a sinusoidal signal of 10 mV at the open circuit potential in 1M solution of KOH. By fitting the Nyquist plots of S1(0.12:1) and V_2CTx with Constant Phase Element (CPE) in series with Randle's model. Furthermore, the resistance of charge transfer for both samples were determined effectively.
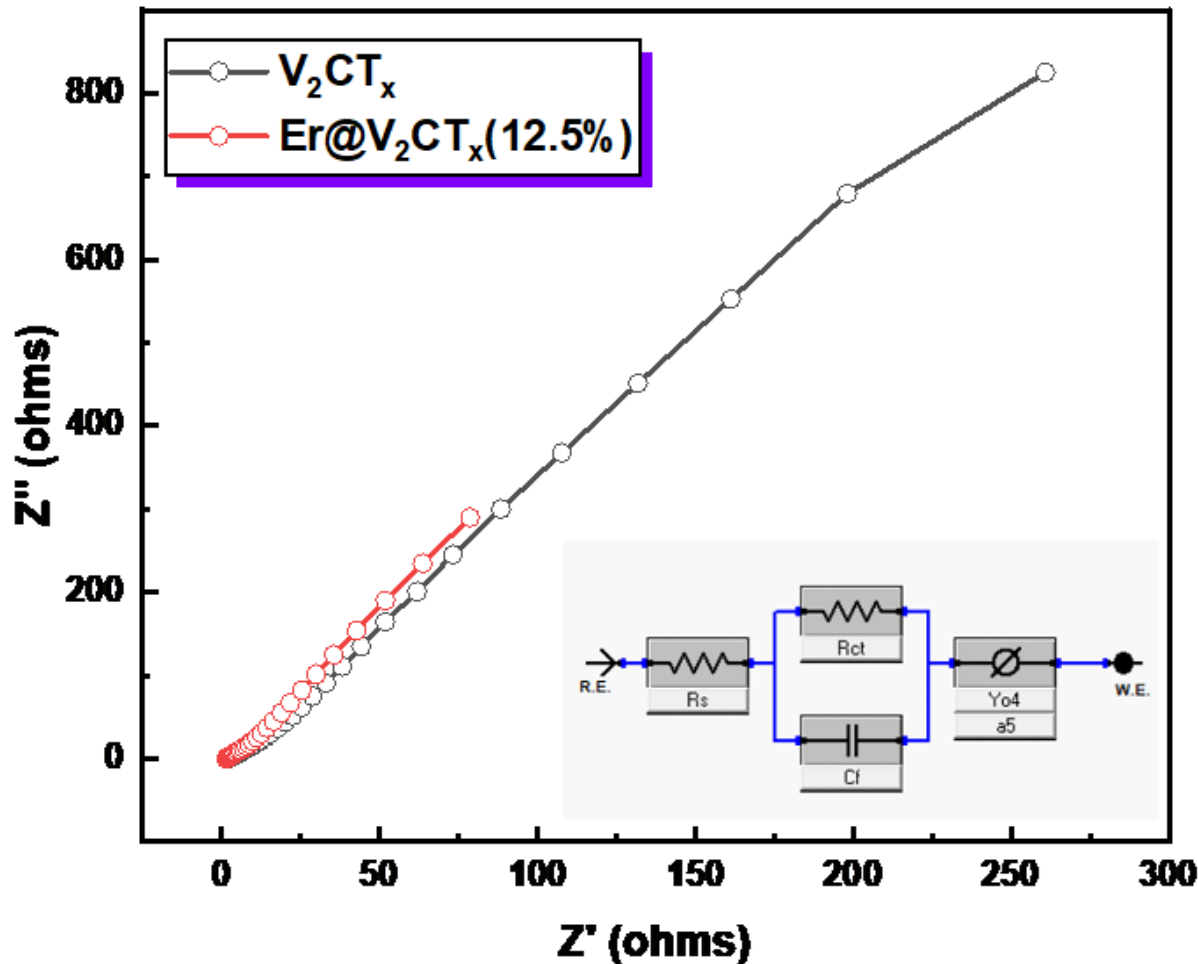
Figure 4.10: Nyquist plot and equivalent circuit for V_2CTx and S1 (0.12:1)

In the inset of the graph, the corresponding circuit diagram is depicted, Rs denotes the ohmic resistance attributed to the electrolyte solution existing between the electrodes of the cell.. R_{ct} signifies the resistance to charge transfer at the electrolyte interface, representing polarization resistance. The parameters W and C_{dl} indicate the Warburg impedance and faradic capacitance, respectively. By observing the Nyquist plot, the diameter of the semicircle reflects the polarization resistance resulting from the faradic reaction at the electrode surface (R_{ct}). Notably, the S1 (0.12:1) nanocomposite demonstrates significantly improved charge transfer behavior compared to the pristine MXene. The polarization resistance for the S1 (0.12:1) nanocomposite measures 1.532 Ω, whereas for V_2CTx it is 1.473 Ω. The solution resistance, or Ohmic resistance, is 2.33 Ω for V_2CTx and 1.567 Ω for the V1 (0.12:1) nanocomposite.

Table 4.2: show the corresponding Rct and Rs of nanocomposite and pristine Mxene

Samples	Rct (Ω)	Rs (Ω)
V$_2$CT$_x$	1.532	2.33
Er@V$_2$CT$_x$ (0.12:1)	1.473	1.567

Chapter 05: Results and Discussion
(Er-Intercalated Ti₃C₂Tₓ MXene)

5. Materials Characterizations
5.1.   X-Ray Diffraction

Figure 5.1 represents the XRD pattern of MAX phase Ti₃SiC₂, pristine Ti₃C₂Tx, and Er@Ti₃C₂ nanocomposites with varying proportions. The MAX phase derived MXene was prepared through the wet etching method. The crystal planes (002) and (103) of Ti₃SiC₂ were identified at 9.95° and 39.6°, respectively. The (002) peak shifted to 9.1°, indicating that Si in Ti₃SiC₂ was removed, yielding Ti₃C₂Tx and an increase in lattice parameter up to 19.4Å. After delamination the (002) peak shift to lower angle of 7.25° and increase in lattic parameter up to 24.3Å. XRD pattern contains peaks corresponding to various phases or compounds present in the sample which provide details about the crystal structure. The attachment of Er to Ti₃C₂Tx sheets altered the XRD pattern of the sample. Specifically, the (002) peak shifted to about 5.75°, which may indicate a change in crystal structure of prepared material is due to chemical composition. The corresponding c-lattice parameter of the (002) peak increased by 30.7 Å for the T1 (0.5:2) nanocomposite.
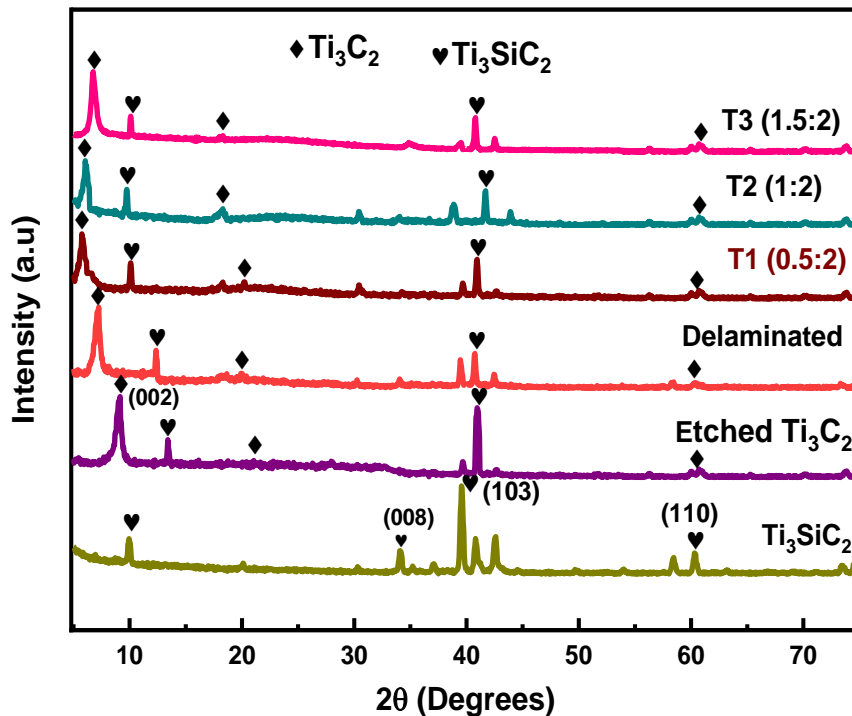
Figure 5.1: XRD of Ti₃SiC₂, Ti₃C₂ and Er@Ti₃C₂ composites

Table 5.1: Show peak shift and c lattice parameters.

Samples	Bragg's Angles	d-spacing (Å)	Lattic Constant (Å)
	2θ	$\dfrac{\lambda}{2\,Sin\,\theta}$	$d_{hkl} * \sqrt{(h^2 + k^2 + l^2)}$
MAX	9.95	8.88	17.7
Etched-Mxene	9.1	9.7	19.4
D-Mxene	7.25	12.18	24.3
T1	5.75	15.35	30.7
T2	6.05	14.5	29.1
T3	6.75	13.08	26.1

5.2. SEM and EDX analysis

Figure 5.2 shows the microstructure analysis of Ti_3SiC_2 MAX phase, Ti3C2TX, and Er@Ti3C2 nanosheets, specifically the T1 (0.5:2) nanocomposite. The figure clearly shows that the nanosheets in Ti3C2TX are distinctly separated and display an impeccable layered structure. Additionally, tiny particles of Er can be observed on the surface of the T1 (0.5:2) nanocomposite.
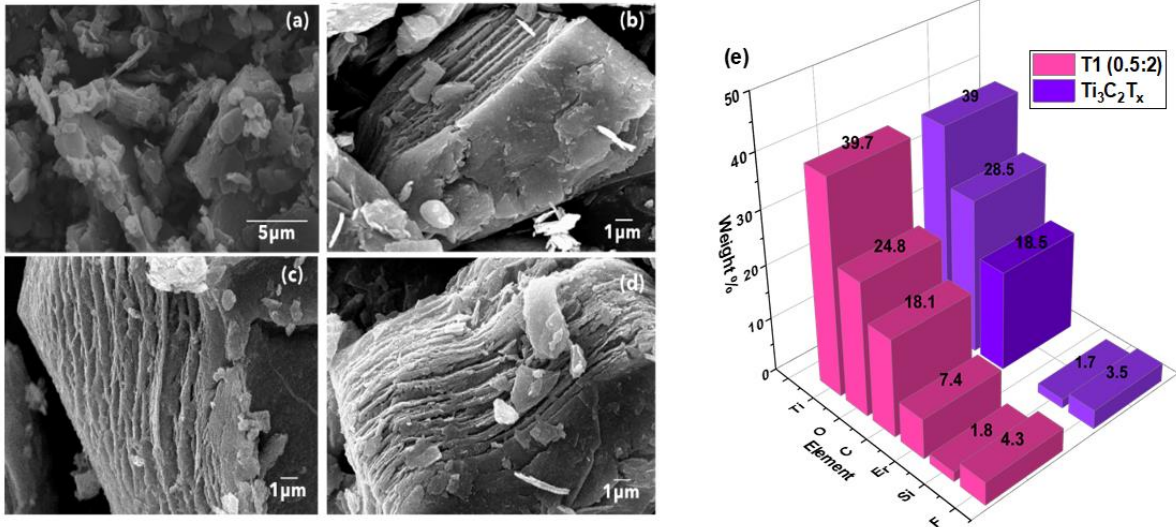
Figure 5.2: *SEM images of a) , b) & c) MXene d) T1 (0.5:2) nanocomposite e) EDX analysis of $Ti_3C_2T_X$ and S1 (0.5:2) nanocomposite*

Figure 5.2e shows the weight percentage of elements present in etched Ti_3C_2Tx and T1 (0.5:2). The lower weight percentage of Si indicates the successful synthesis of Ti_3C_2Tx MXene from the precursor Ti_3SiC_2 MAX phase. Furthermore, the presence of Er in the T1 (0.5:2) nanocomposite confirms the successful synthesis of the sample.

5.3.   FTIR analysis

Figure 5.3 represents the FTIR spectra of etched Ti_3C_2Tx. In spectra, observed broad absorption bands observed at 3430 cm^{-1} which shows the vibrational stretching of hydroxyl group (–OH) and peak at 2923 cm^{-1} corresponds to C-H bond. The O-H vibrational mode is represented around 1630 cm^{-1}, and the bands in the fingerprint region the peak at correspond to 1019 cm^{-1} C-F bond and 648 cm^{-1} is associated to the and Ti-O stretching band.
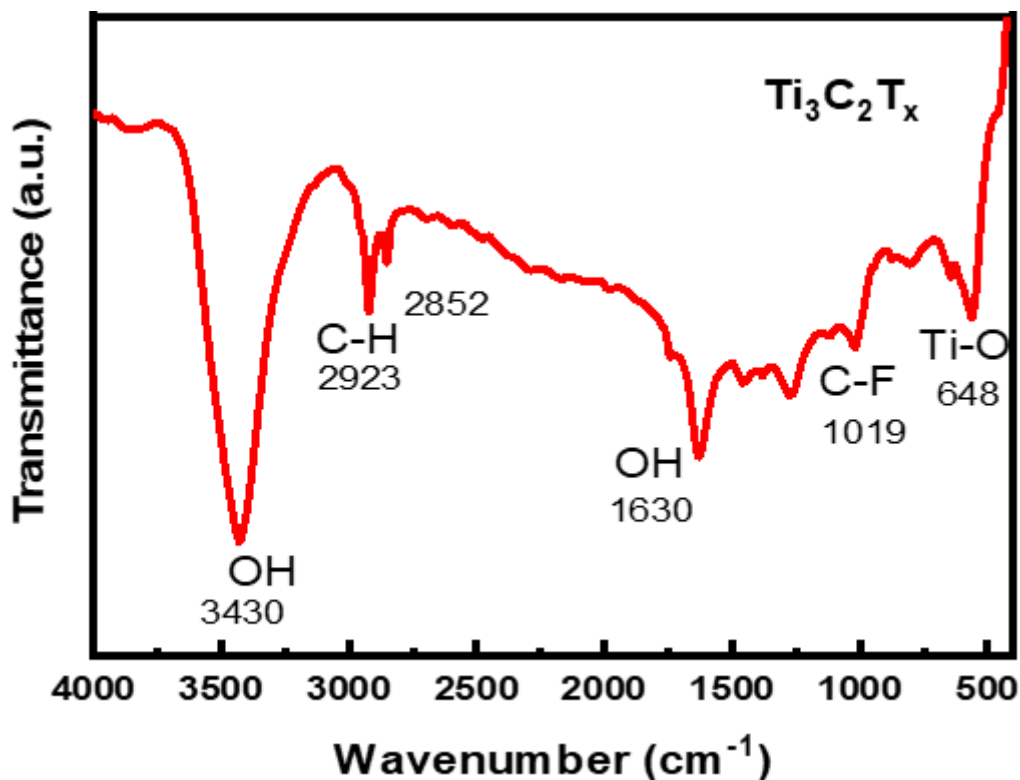
Figure 5.3: Representation of FTIR spectra of **Ti₃C₂Tx** MXene

Similarly, Figure 5.4 illustrates the FTIR spectra of T1(0.5:1) nanocomposite, where absorption bands at 3423 cm^{-1}, 2924 cm^{-1}, 2850 cm^{-1}, 1633 cm^{-1}, 1024 cm^{-1} and 510 cm^{-1} can be observed. At 3423 cm^{-1} broad band corresponds to the –OH vibrational stretching, The bands at 2924 cm^{-1} and 2850 cm^{-1} correspond to the C-H vibrational stretching vibrations. while the peak at 1633 cm^{-1} represents O-H bending vibrations. The bands at 1024 cm^{-1} and 645 cm^{-1} are relevant to the C-F and Ti-O stretching mode, respectively. Additionally, there is a prominent peak of Er-O characteristic vibration at 510 cm^{-1}.
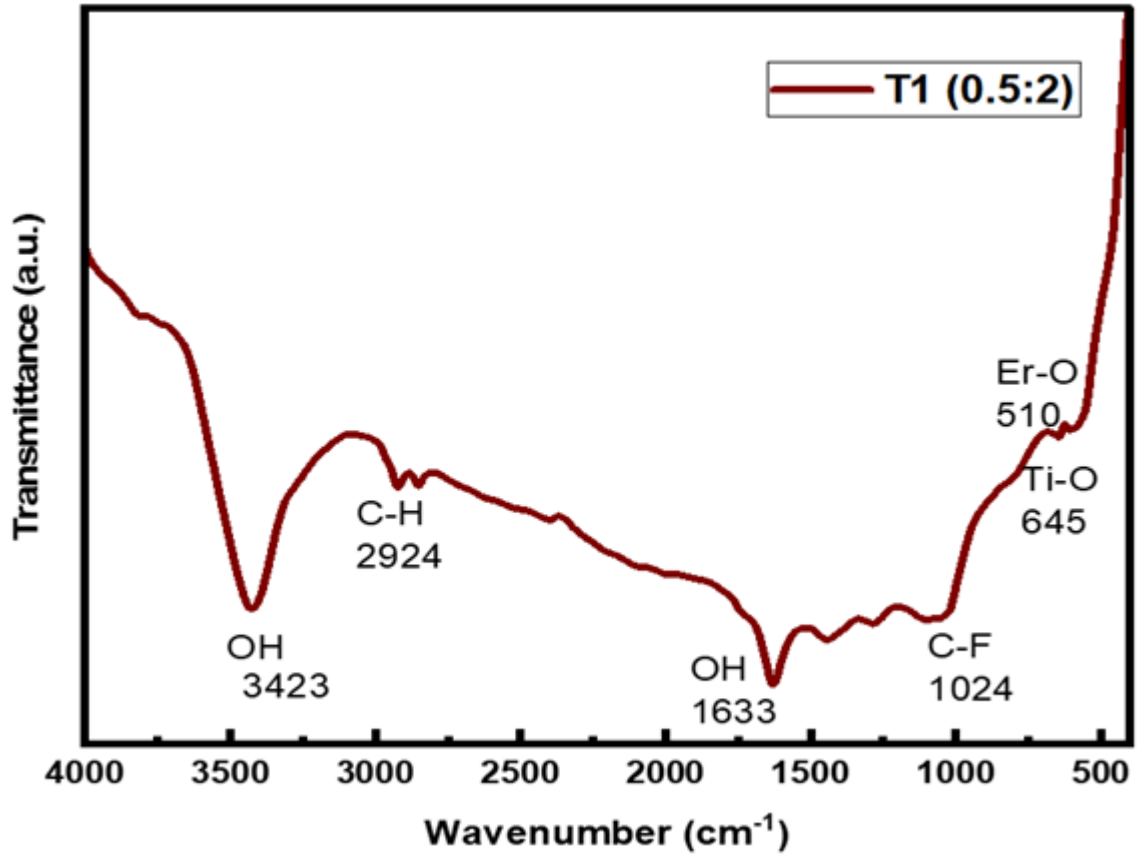
Figure 5.4: Representation of FTIR spectra of **T1 (0.5:2)**

5.4.   Raman Spectroscopy

The Raman spectra of Ti_3SiC_2 MAX phase, delaminated Ti_3C_2Tx MXene powder and Er@Ti_3C_2Tx shown in figure 5.5. The MAX phase characteristic peaks are identified at 151 cm^{-1}, 235 cm^{-1}, 397 cm^{-1}, and 603 cm^{-1}. The Raman spectra of Ti_3C_2Tx MXene shows an A1g mode at 151 cm^{-1} which assigned to TiSi atoms vibrations. The subsequent vibration contains surface groups, Si, and C atomic planes. In addition, the Ti_2 atoms in-plane and out-of-plane vibrations of the outer layer also attached with functional groups and carbon atoms are identified at 235 cm^{-1} and 397 cm^{-1} respectively. It related to the phonon modes Eg (Ti, C, O) and A1g (Ti, C, O). Observation of phonon peak at 603 cm^{-1} confirm the Eg and A1g vibrations of C atoms[70]. Peak shifting in position is observed when both data are compared. The upshifting of the peak's position is attributed to the elongation of bonds. The structural atomic strain is also linked to the prolongation of bonds. The Raman data also shows the M-Tx bond stretching or weakening due to the shielding effect of the Er atom as it attaches at the surface.
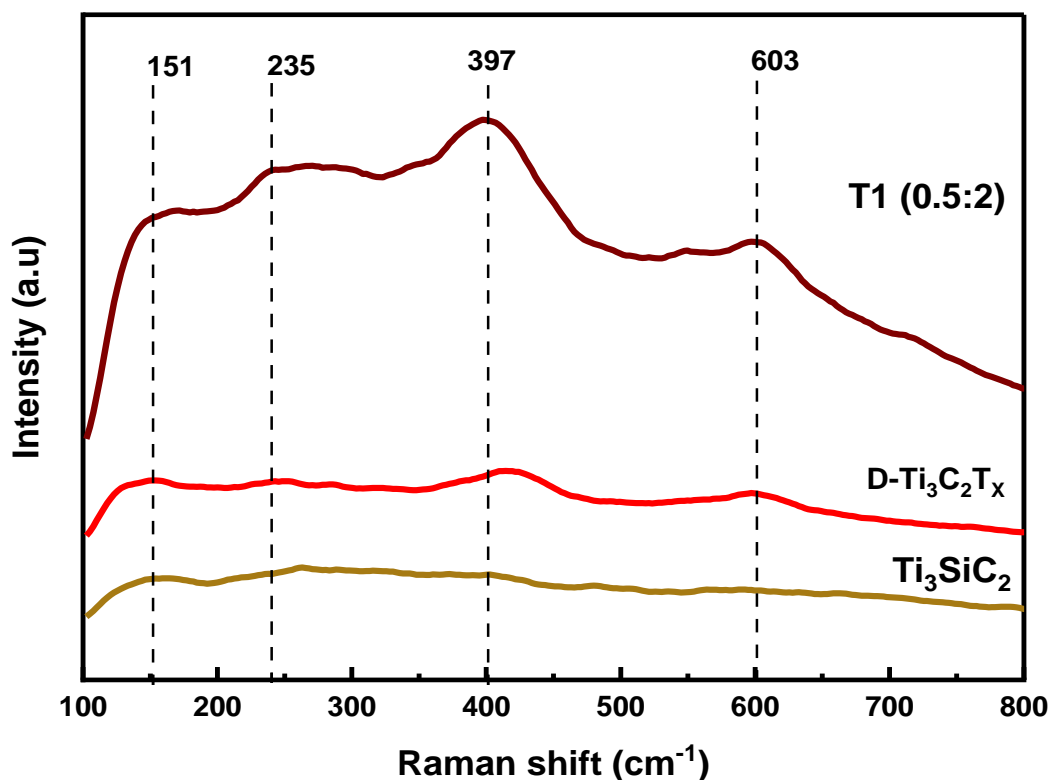
Figure 5.5: Raman spectra of MAX, delaminated MXene and T1 (0.5:2)

5.5. Electrochemical Analysis and measurements

5.5.1. Linear Sweep Voltammetry (LSV)

The Nernst equation, E RHE = E Ag /AgCl + 0.0591pH + 0.205, was used to analyze all potentials in LSV in reversible hydrogen electrode (RHE), and both the OER and the HER were studied at a fixed scan rate of 10 mVs^{-1}.

Ti_3C_2Tx and $Er@Ti_3C_2Tx$ Composites:

Composites of Ti_3C_2Tx were prepared with Er in different mass ratios i-e 0.5:2, 1:2 and 1.5:2. MXene and Er: MXene samples were synthesized and labelled as T1, T2, T3. Among all these ratios $Er@Ti_3C_2Tx$ (0.5:2) denoted as T1 gave best results for overall water splitting applications in 1M KOH.

5.5.2. Oxygen Evolution Reaction (OER)

The OER activity of Ti_3C_2Tx and $Er@Ti_3C_2Tx$ nanocomposites was accessed using a standard three-electrode system in a 1M KOH electrolyte. The Nickle foam mass loading was 1.0 mg-cm^{-2} and with a set potential of 0 to 0.4V and scan rate 10 mVs^{-1}. The T1 (0.5:2) nanocomposite exhibited the highest activity, the lowest onset potential, the lowest

overpotential η_{10} (381mV) and the least Tafel slope of 157mVdec^{-1} .The other electrocatalysts Ti$_3$C$_2$Tx, T2 (1:2), and T3 (1.5:2) showed overpotentials of 550mV, 480mV and 410mV, respectively, at the same current density of 10mAcm^{-2} and Tafel slopes of 504 mVdec^{-1}, 282mVdec^{-1} and 183 mVdec^{-1} respectively.
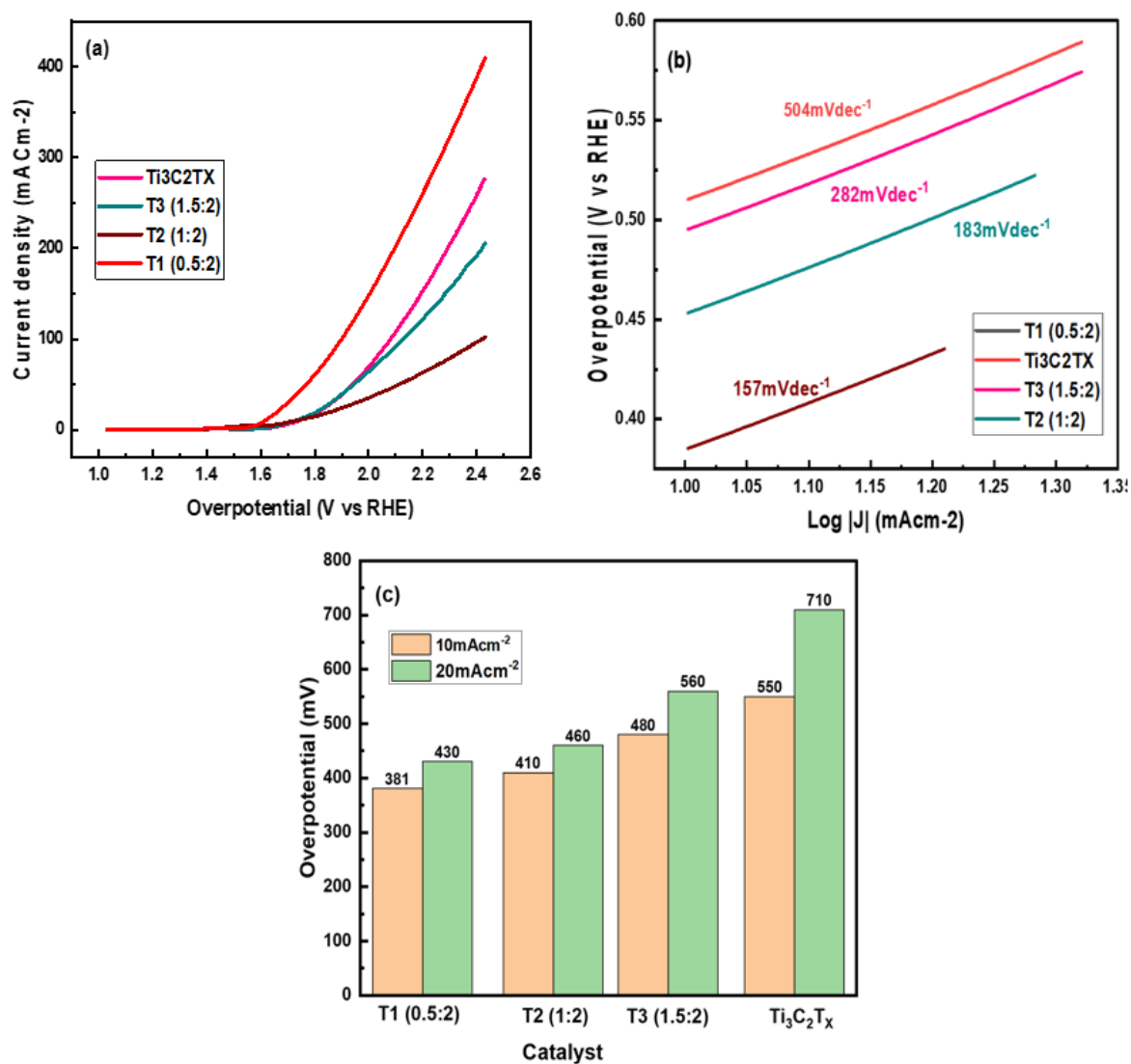
Figure 5.6: a) OER Polarization Curves **b)** Tafel slope for T1,t2,T3 and Ti$_3$C$_2$T$_X$ **c)** Overpotential at 10mAcm^{-2} and 20mAcm^{-2} for T1, T2,T3 and Ti$_3$C$_2$T$_X$

5.5.3. Hydrogen Evolution Reaction Performance

The process of Hydrogen evolution reaction (HER) reaction generally occurs in the alkaline electrolytes. It typically begins with a phase where water dissociates and forms a proton (H$^+$) adsorbed on the surface of electrode which is known as Volmer step (figure 5.7 a). Then, it was followed by the Tafel step where adsorbed species recombine or absorbance of water molecules with hydrogen draw in coupling and the Heyrovsky step following by the electron. The electrochemical desorption occurred and it created the molecular hydrogen at

the electrode surface M in result of Heyrovsky step. The T1 nanocomposite follows the Volmer-Heyrovsky pathway for the HER process during rate determining step (RDS) according to literature as well as indicated by its slope value.

The reaction is followed as:

$$H2O + M + e- \rightarrow MHads + OH- \qquad .....\textbf{Volmer Step: 120 mV dec}^{-1}$$

$$MHads + H2O + e- \rightarrow H2 + M + OH- \quad .....\textbf{Heyrovsky Step: (40 mV dec}^{-1}$$
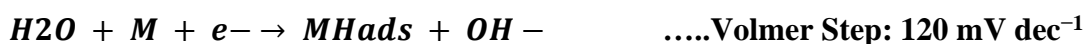
Tafel slope values are represented in figure 5.7 b and the values T1, T2 and T3 observed 102, 164 and 176 mV-dec^{-1} respectively. Whereas, T1 has 102 mV/dec which is lowest. Furthermore, the Tafel slopes of pure Ti$_3$C$_2$Tx are 201 mV dec^{-1} respectively. By using the nickel foam substrate, cause significant enhancement in the overall performance of the T1 nanocomposite could be due to the Er strong interaction with Ti$_3$C$_2$Tx on a nickel foam substrate. The nickel substrate in the composite structure acts as a conductive support and facilitating a fast transfer channel for electron-mass. Additionally, the nickel foam has demonstrated very low activity for OER and HER, indicating that it has a negligible impact on the entire water splitting process.

The flow of electrolytic ions into the active sites of sample by phenomena of creating the narrow path could be stimulated by using the porous nickel materials. Additionally, the robust bonding of Er onto MXene nanosheets, coupled with the active sites of Er, has resulted in improved electrochemical performance. XRD analysis showed that the intercalation of Er into MXene layers facilitated faster ion diffusion pathways. The interaction between the surface oxygen at Ti$_3$C$_2$Tx and H is quite strong which impedes the escape of H$_2$ gas. This interaction also enhanced the capability of Ti$_3$C$_2$Tx and expedites the charge transfer process. Figure **5.7 c** shows the overpotential exhibited by all studied materials.
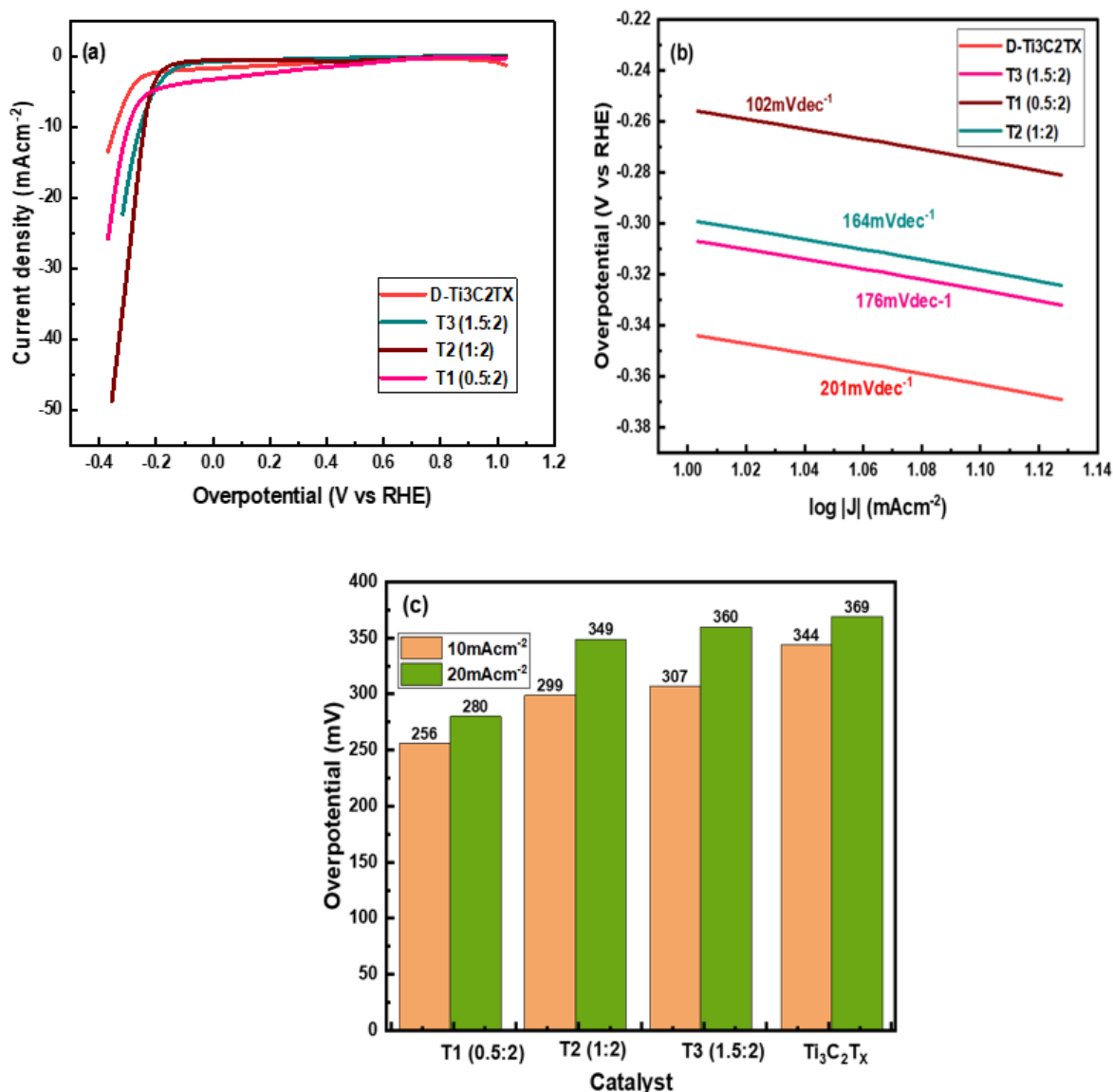
Figure 5.7: a) HER Polarization Curves **b)** Tafel slope for T1,T2,T3 a $Ti_3C_2T_X$ **c)** Overpotential at 10 mAcm^{-2} and 20mAcm^{-2} for T1, T2,T3 and $Ti_3C_2T_X$

5.6. Electrochemical Impedance Spectroscopy (EIS)

The technique Electrochemical impedance spectroscopy (EIS) was utilized to study the mechanism in which involve the electron transport. Figure 5.5 represents the EIS patterns of pristine Ti3C2Tx and Er@Ti3C2Tx structure and comparable circuit model. Then, a simple Randle model with constant phase element was used in series for EIS data. The diffusion impedance was calculated by employing the constant phase element in series with Randle cell and Table 5.2 representing the fitting parameters.

The electron transfer resistance (Rct) was found in the following order**:** $Ti_3C_2Tx >$ Er@Ti$_3C_2$Tx structure with Rct values of 342.7 > 290 respectively. These findings confirm

the significantly improved conductivity of Ti_3C_2Tx MXene and its faster transfer mechanism leading to more rapid reaction kinetics. In a reduction of charge transfer resistance (Rct) to 290 Ω for T1 nanocomposite compared to pristine Ti_3C_2Tx (342.7 Ω) resulted by the Nyquist plot. That indicates the stimulation of electron transport from the catalyst to the electrolyte and improved conductivity due to the strong coupling of Ti_3C_2Tx MXene with T1 nanocomposite. Overall, the catalytic performance is enhanced by the phenomenon of increasing number of electrochemically active sites.
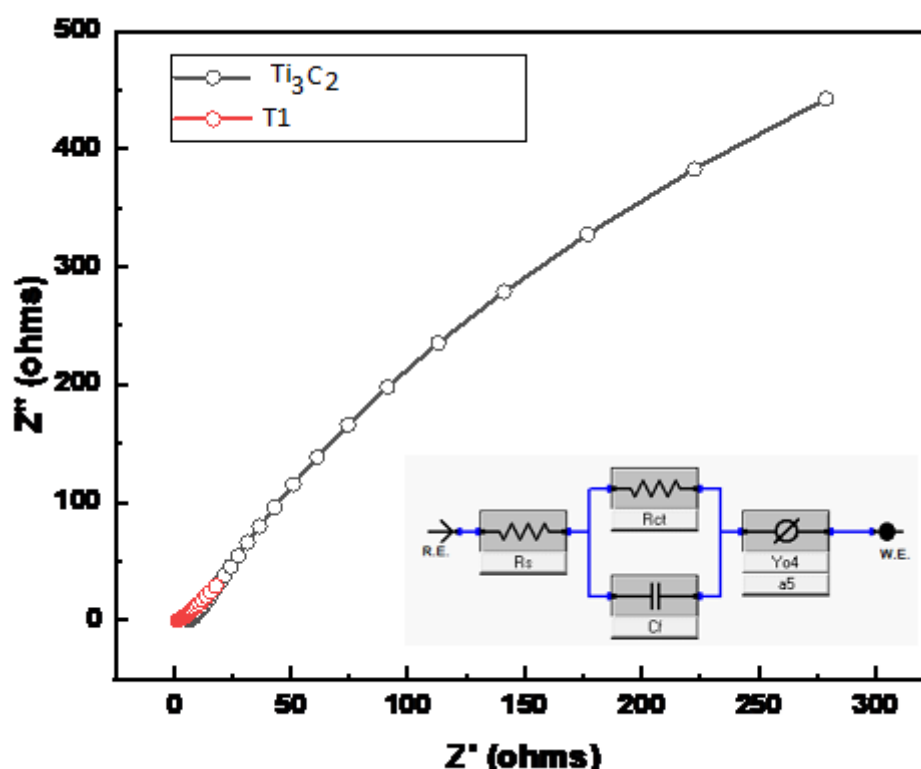
Figure 5.8: a) Nyquist plots **b)** Chronoamperometry of Ti_3C_2Tx and T1 (0.12:1)

Table 5.2: Resistant values from Nyquist plot

Samples	Rct (Ω)	Rs (Ω)
Ti₃C₂Tx	342.7	6.731
Er@Ti₃C₂Tx (T1)	294.0	1.767

The Nyquist plots are represented in figure 5.8 (a) for pristine Ti_3C_2Tx MXene and T1 composite at frequencies ranging from 0.1 kHz to 20 kHz. (b) Comparison of charge transfer

resistance corresponding to pristine $Ti_3C_2T_x$ MXene and T1 composite calculated using equivalent circuit model. (c) The equivalent circuit utilized to demonstrate the Nyquist plots corresponding to pristine $Ti_3C_2T_x$ MXene and T1 composite at frequencies ranging from 0.1 kHz to 20 kHz.

EIS is also an important technique to understand the OER reaction kinetics. The T1 composite showed the lowest charge transfer resistance of only 342.7 ohm in comparison to other materials and higher kinetics as represented in figure. 5.8

This could be happened due to the synergistic electrical conductivity of composite with layered structure and high specific surface area.

5.7. Stability Test

5.7.1. Chronoamperometry

Maintaining the stability of electrochemical materials is critical element for their commercial applications. Figure 5.9 represents the stability of pristine $Ti_3C_2T_x$ MXene and T1 composite sample by chronoamperometry test which performed at 0.6 V. The relative current stability of 80% and 34% was observed after 14 hours of operation for T1 nanocomposite and pristine $Ti_3C_2T_x$ MXene respectively which indicating the stable behavior attributed to the material's structural features. During chronoamperometry testing, ion diffusion resistance was observed to reduce at the interface of electrode-electrolyte which facilitated the penetration of ion via the active sites in the prepared material due to the electrochemical activation process.
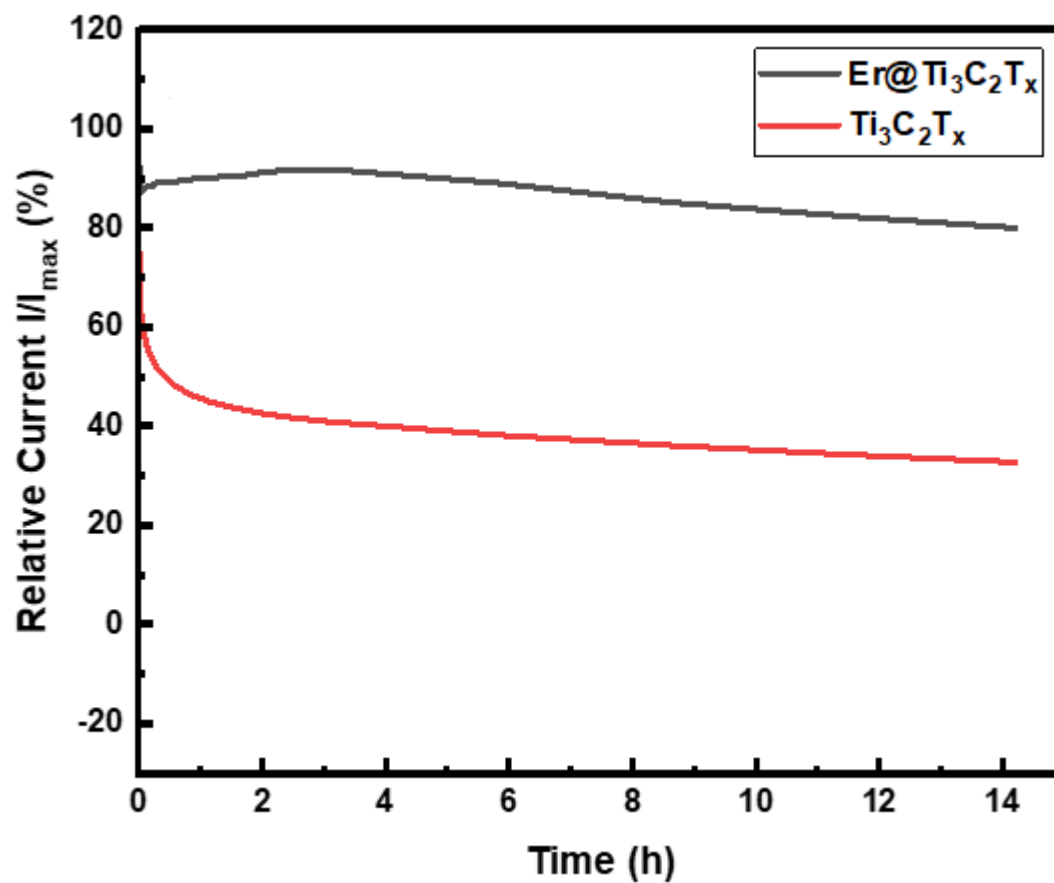
Figure 5.9: Stability measurements of T1(0.5:1) and Ti_3C_2Tx MXene

Chapter 6: Conclusion and Future Work

6. Conclusion

The two-dimensional MXene, also known as transition metal carbide, was created in this study by wet etching route, treating a three-dimensional MAX phase with hydrofluoric acid. MXene is a member of the P63/mmc space group and has a hexagonal structure. The generic formula for MXene is Mn+1XnTx is, where M is an early transition metal, Tx is the surface termination that is attached when MXene is etched from the MAX phase, and X is either nitrogen or carbon. Additionally, Er particles were successfully hosted by V_2CTx and Ti_3C_2Tx sheets using as an easy approach. Er@V_2CTx of mass ratio 0.12:1, referred to as S1, stands out as being more effective than the other nanocomposites whereas Er@Ti_3C_2Tx having mass ratio 0.5:2, denoted as T1 gives best results. The V_2CTx offers conductive surface area and encourages erbium atom's distributed growth on its surface, which enhances reaction kinetics and lessens ion transport barriers. The nanocomposite was employed as an electrocatalyst for HER and OER yielding good catalytic activities. Er addition significantly raises the activation energy, decreases the critical voltage, and improves the ionic conductivity of MXenes, all of which are distinguishing characteristics of its catalytic efficacy. For HER, the Er@V_2CTx and Er@Ti_3C_2Tx electrocatalysts provide a small overpotential of 174mV and 256mV at current density of $10mAcm^{-2}$ and a minimal Tafel slope of $107mVdec^{-1}$ and $102mVdec^{-1}$ was achieved, respectively. During OER, both the electrocatalyst Er@V_2CTx and Er@Ti_3C_2Tx at $10mAcm^{-2}$ recorded an overpotential of 370mV and 381mV respectively with a Tafel slope of $131mVdec^{-1}$ and $157mVdec^{-1}$. MXene powders and nanocomposite were electrochemically analyzed in 1M KOH with Ag/AgCl as the reference electrode and platinum wire as the counter electrode. Chronoamperometry test shows that both the electrocatalyst exhibit excellent catalytic performance, stability, and showed better durability. The XRD peaks of Er@V_2CTx and Ti_3C_2Tx nanocomposite peaks were found to shift to a lower angle and alter in peak strength using the XRD technique, showing that the c-lattice parameter increased. SEM, EDS, FTIR, and Raman were used to further characterize the sample and examine the morphology and properties of pure MXene and Er@MXene nanocomposite. This research offers a quick, straightforward, and inexpensive way to make MXene composite using nitrate. It also gives researchers the opportunity to investigate the various uses of MXene composites, including those in supercapacitors and general water splitting.

References

1. What Is Nanotechnology? | National Nanotechnology Initiative.
    https://www.nano.gov/nanotech-101/what/definition.

2. nanoscale materials - Yahoo Search Results.
    https://search.yahoo.com/search;_ylt=Awr.zZXmXGRkAzwHKEBXNyoA;_ylc=X1M
    DMjc2NjY3OQRfcgMyBGZyA21jYWZlZQRmcjIDc2ItdG9wBGdwcmlkA0FvTnFz
    WXQuVGVtaldzZ1ZDZXp4RkEEbl9yc2x0AzAEbl9zdWdnAzUEb3JpZ2luA3NlYXJ
    jaC55YWhvby5jb20EcG9zAzAEcHFzdHIIDBHBxc3RybAMwBHFzdHJsAzIwBHF1
    ZXJ5A25hbm9zY2FsZSUyMG1hdGVyaWFscyUyMAR0X3N0bXADMTY4NDI5O
    TI5NQ--?p=nanoscale+materials+&fr2=sb-top&fr=mcafee&type=E210US91215G0.

3. Dew-Hughes, D. The critical current of superconductors: an historical review. *Low
    Temp. Phys.* **27**, 713–722 (2001).

4. Electrical Resistance of Metals - George T. Meaden - Google Books.
    https://books.google.com.pk/books?hl=en&lr=&id=UFv0BwAAQBAJ&oi=fnd&pg=P
    R9&dq=electrical+resistance+&ots=2KrTYw-Ib5&sig=IgjpT02m-VbJ_t-
    7uvz91WLCj74&redir_esc=y#v=onepage&q=electrical resistance&f=false.

5. Cornell, R. M. & Schwertmann, U. The Iron Oxides. *Iron Oxides* (2003)
    doi:10.1002/3527602097.

6. Feynman, R. P. There's plenty of room at the bottom. *J. Microelectromechanical Syst.*
    1, 60–66 (1992).

7. Drexler, K. E. Nanotechnology: From Feynman to Funding.
    http://dx.doi.org/10.1177/0270467604263113 **24**, 21–27 (2004).

8. Binnig, G., Quate, C., letters, C. G.-P. review & 1986, undefined. Atomic force
    microscope. *APS*.

9. Binnig, G., Quate, C. F. & Gerber, C. Atomic force microscope. *Phys. Rev. Lett.* **56**,
    930–933 (1986).

10. Schaming, D. & Remita, H. Nanotechnology: from the ancient time to nowadays.
    Found. Chem. **17**, 187–205 (2015).

11. Serrano, E., Rus, G. & García-Martínez, J. Nanotechnology for sustainable energy.
    Renew. Sustain. Energy Rev. **13**, 2373–2384 (2009).

12.   Geim, A. K. Graphene: Status and prospects. *Science (80-.).* **324**, 1530–1534 (2009).

13.   Two-dimensional MXene-based and MXene-derived photocatalysts: Recent developments and perspectives - ScienceDirect. https://www.sciencedirect.com/science/article/pii/S1385894720342157.

14.   Zhong, Q., Li, Y. & Zhang, G. Two-dimensional MXene-based and MXene-derived photocatalysts: Recent developments and perspectives. *Chem. Eng. J.* **409**, 128099 (2021).

15.   Giesecke, K., Goldberg, L. R. & Ding, X. A Top-Down Approach to Multiname Credit. *https://doi.org/10.1287/opre.1100.0855* **59**, 283–300 (2010).

16.   Murugavel, R., Walawalkar, M. G., Dan, M., Roesky, H. W. & Rao, C. N. R. Transformations of molecules and secondary building units to materials: A bottom-up approach. *Acc. Chem. Res.* **37**, 763–774 (2004).

17.   Woodberry, A. N. & Mensah, F. E. Applications of Nanomaterials in Nanomedicine. *Spectrosc. Charact. Nanomater. Nov. Mater.* 345–360 (2022) doi:10.1002/9783527833689.CH14.

18.   Geonmonond, R. S., Da Silva, A. G. M. & Camargo, P. H. C. Controlled synthesis of noble metal nanomaterials: Motivation, principles, and opportunities in nanocatalysis. *An. Acad. Bras. Cienc.* **90**, 719–744 (2018).

19.   Gregorczyk, K. & Knez, M. Hybrid nanomaterials through molecular and atomic layer deposition: Top down, bottom up, and in-between approaches to new materials. *Prog. Mater. Sci.* **75**, 1–37 (2016).

20.   Buzea, C. & Pacheco, I. Nanomaterials and their classification. *Adv. Struct. Mater.* **62**, 3–45 (2017).

21.   Tiwari, J. N., Tiwari, R. N. & Kim, K. S. Zero-dimensional, one-dimensional, two-dimensional and three-dimensional nanostructured materials for advanced electrochemical energy devices. *Prog. Mater. Sci.* **57**, 724–803 (2012).

22.   Lee, K., Mazare, A. & Schmuki, P. One-dimensional titanium dioxide nanomaterials: Nanotubes. *Chem. Rev.* **114**, 9385–9454 (2014).

23. Fu, S., Sun, Z., Huang, P., Li, Y. & Hu, N. Some basic aspects of polymer

nanocomposites: A critical review. *Nano Mater. Sci.* **1**, 2–30 (2019).

24. Timoshenko, J., Lu, D., Lin, Y. & Frenkel, A. I. Supervised Machine-Learning-Based Determination of Three-Dimensional Structure of Metallic Nanoparticles. *J. Phys. Chem. Lett.* **8**, 5091–5098 (2017).

25. Poh, T. Y. *et al.* Inhaled nanomaterials and the respiratory microbiome: Clinical, immunological and toxicological perspectives. *Part. Fibre Toxicol.* **15**, (2018).

26. Choi, W. *et al.* Recent development of two-dimensional transition metal dichalcogenides and their applications. *Mater. Today* **20**, 116–130 (2017).

27. Zhao, J. *et al.* Rise of silicene: A competitive 2D material. *Prog. Mater. Sci.* **83**, 24–151 (2016).

28. Golberg, D. *et al.* Boron nitride nanotubes and nanosheets. *ACS Nano* **4**, 2979–2993 (2010).

29. Barsoum, M. W. & Radovic, M. Elastic and Mechanical Properties of the MAX Phases. *https://doi.org/10.1146/annurev-matsci-062910-100448* **41**, 195–227 (2011).

30. Mathis, T. S. *et al.* Modified MAX Phase Synthesis for Environmentally Stable and Highly Conductive Ti3C2MXene. *ACS Nano* **15**, 6420–6429 (2021).

31. Naguib, M., Barsoum, M. W. & Gogotsi, Y. Ten Years of Progress in the Synthesis and Development of MXenes. *Adv. Mater.* **33**, (2021).

32. Anasori, B. & Gogotsi, Y. 2D Metal carbides and nitrides (MXenes): Structure, properties and applications. *2D Met. Carbides Nitrides Struct. Prop. Appl.* 1–534 (2019) doi:10.1007/978-3-030-19026-2/COVER.

33. Hong Ng, V. M. *et al.* Recent progress in layered transition metal carbides and/or nitrides (MXenes) and their composites: synthesis and applications. *J. Mater. Chem. A* **5**, 3039–3068 (2017).

34. Fan, Y. *et al.* Recent Advances in Growth of Transition Metal Carbides and Nitrides (MXenes) Crystals. *Adv. Funct. Mater.* **32**, (2022).

35. Wang, S., Yang, X., Zhou, L., Li, J. & Chen, H. 2D nanostructures beyond graphene: preparation, biocompatibility and biodegradation behaviors. *J. Mater. Chem. B* **8**, 2974–2989 (2020).

36. Pei, Y. *et al.* Ti3C2TXMXene for Sensing Applications: Recent Progress, Design Principles, and Future Perspectives. *ACS Nano* **15**, 3996–4017 (2021).

37. IAS @ oneclick: Nano Technology for IAS. https://prakashhiremathias.blogspot.com/2016/02/nano-technology-for-ias.html.

38. Super Capacitors - Elon's Secret? : r/teslamotors. https://www.reddit.com/r/teslamotors/comments/5kkfmc/super_capacitors_elons_secret/.

39. Zhu, Y. *et al.* Structural Engineering of 2D Nanomaterials for Energy Storage and Catalysis. *Adv. Mater.* **30**, 1706347 (2018).

40. Gao, L. *et al.* Preparation and performance of MAX phase Ti3AlC2 by in-situ reaction of Ti-Al-C system. *Adv. Powder Technol.* **31**, 3533–3539 (2020).

41. Zhang, L. ; *et al.* Influencing Factors on Synthesis and Properties of MXene: A Review. *Process. 2022, Vol. 10, Page 1744* **10**, 1744 (2022).

42. VahidMohammadi, A., Kayali, E., Orangi, J. & Beidaghi, M. Techniques for MXene delamination into single-layer flakes. *2D Met. Carbides Nitrides Struct. Prop. Appl.* 177–195 (2019) doi:10.1007/978-3-030-19026-2_11/COVER.

43. Hasan, M. M., Hossain, M. M. & Chowdhury, H. K. Two-dimensional MXene-based flexible nanostructures for functional nanodevices: a review. *J. Mater. Chem. A* **9**, 3231–3269 (2021).

44. Jiang, J. *et al.* Intercalation engineering of MXenes towards highly efficient photo(electrocatalytic) hydrogen evolution reactions. *J. Mater. Chem. A* **9**, 24195–24214 (2021).

45. Lei, J. C., Zhang, X. & Zhou, Z. Recent advances in MXene: Preparation, properties, and applications. *Front. Phys.* **10**, 276–286 (2015).

46. Chen, J. *et al.* Recent progress and advances in the environmental applications of MXene related materials. *Nanoscale* **12**, 3574–3592 (2020).

47. Bai, X. *et al.* Insight into the catalytic activity of MXenes for hydrogen evolution reaction. *Sci. Bull.* **63**, 1397–1403 (2018).

48. Harrison, K. & Levene, J. I. Electrolysis of water. *Sol. Hydrog. Gener. Towar. a*

Renew. Energy Futur. 41–63 (2008) doi:10.1007/978-0-387-72810-0_3/COVER.

49.   Wang, Q. & Domen, K. Particulate Photocatalysts for Light-Driven Water Splitting:
       Mechanisms, Challenges, and Design Strategies. *Chem. Rev.* **120**, 919–985 (2020).

50.   Nørskov, J. K. *et al.* Origin of the overpotential for oxygen reduction at a fuel-cell
       cathode. *J. Phys. Chem. B* **108**, 17886–17892 (2004).

51.   Burkan Isgor, O., Ge, J., Ge, J. & Isgor, O. B. Effects of Tafel slope, exchange current
       density and electrode potential on the corrosion of steel in concrete. *Mater. Corros.* **58**,
       573–582 (2007).

52.   Li, Y., Zhou, L. & Guo, S. Noble metal-free electrocatalytic materials for water
       splitting in alkaline electrolyte. *EnergyChem* **3**, 100053 (2021).

53.   Park, S. *et al.* Reducing the high hydrogen binding strength of vanadium carbide
       MXene with atomic Pt confinement for high activity toward HER. *Appl. Catal. B
       Environ.* **304**, 120989 (2022).

54.   Zahra, S. A. & Rizwan, S. MWCNT-modified MXene as cost-effective efficient
       bifunctional catalyst for overall water splitting. *RSC Adv.* **12**, 8405–8413 (2022).

55.   Kim, K. K. *et al.* FeNi LDH/V2CTx/NF as Self-Supported Bifunctional Electrocatalyst
       for Highly Effective Overall Water Splitting. *mdpi.com* (2022)
       doi:10.3390/nano12152640.

56.   Wang, J. *et al.* Well-dispersed ultrafine Pt nanoparticles anchored on oxygen-rich
       surface of V2CTx (MXene) for boosting hydrogen evolution reaction. *Elsevier*.

57.   Wang, J., Liu, Y. & Yang, G. Cobalt decorated ultra-thin Ti3C2 MXene electrocatalyst
       for high-efficiency hydrogen evolution reaction. *Mater. Res. Express* **6**, (2019).

58.   Huang, L. *et al.* Hierarchical MoS2 nanosheets integrated Ti3C2 MXenes for
       electrocatalytic hydrogen evolution. *Elsevier*.

59.   Ashraf, I., Ahmad, S., Rizwan, S. & Iqbal, M. Fabrication of Ti3C2@MoO3
       nanocomposite as an electrode material for highly efficient and durable water splitting
       system. *Fuel* **299**, (2021).

60.   Jović, V. D., Zejnilović, R. M., Despić, A. R. & Stevanović, J. S. Characterization of
       electrochemically formed thin layers of binary alloys by linear sweep voltammetry. *J.*

Appl. Electrochem. **18**, 511–520 (1988).

61. Magar, H. S., Hassan, R. Y. A. & Mulchandani, A. Electrochemical Impedance Spectroscopy (EIS): Principles, Construction, and Biosensing Applications. *Sensors 2021, Vol. 21, Page 6578* **21**, 6578 (2021).

62. Lantelme, F. & Chemla, M. Chronoamperometry for the determination of metallic interdiffusion coefficients. Rapid transport processes in the first atomic layers. *J. Electroanal. Chem.* **396**, 203–209 (1995).

63. Kafle, B. P. Introduction to nanomaterials and application of UV–Visible spectroscopy for their characterization. *Chem. Anal. Mater. Charact. by Spectrophotometry* 147–198 (2020) doi:10.1016/B978-0-12-814866-2.00006-3.

64. Baradaran-Ghandi, M., International, S. H.-T.-C. & 2018, undefined. Mechanochemical self-explosive synthesis and characterization of Mo-V2C nanocomposite. *Elsevier*.

65. Baradaran-Ghandi, M. H. & Hassanzadeh-Tabrizi, S. A. Mechanochemical self-explosive synthesis and characterization of Mo-V2C nanocomposite. *Ceram. Int.* **44**, 5447–5452 (2018).

66. Zhang, Y., Lu, W. Bin, Zhou, J. P., Sun, D. Q. & Li, H. M. Facile self-assembly of sandwich-like MXene V2CTx/Ag/rGO/MWCNTs layered multiscale structure nanocomposite. *Ceram. Int.* **49**, 1911–1921 (2023).

67. Zhang, Y., Lu, W. Bin, Zhou, J. P., Sun, D. Q. & Li, H. M. The multiple synthesis of layered V2CTx-MXene composites with enhanced electrochemical properties. *J. Alloys Compd.* **929**, 167276 (2022).

68. Yoneyama, H., Sakamoto, H., Acta, H. T.-E. & 1975, undefined. A Photo-electrochemical cell with production of hydrogen and oxygen by a cell reaction. *Elsevier*.

69. Darband, G., Aliofkhazraei, M., … S. H.-J. of P. & 2019, undefined. Electrodeposited NiCoP hierarchical nanostructure as a cost-effective and durable electrocatalyst with superior activity for bifunctional water splitting. *Elsevier*.

70. Sarycheva, A. & Gogotsi, Y. Raman Spectroscopy Analysis of the Structure and Surface Chemistry of Ti3C2T xMXene. *Chem. Mater.* **32**, 3480–3488 (2020).